Multi-Objective Flight Control for Ride Quality Improvement for Flexible Aircraft

Nhan Nguyen*
Kelley Hashemi†
NASA Ames Research Center, Moffett Field, CA 94035

This paper describes a multi-objective flight control system design for ride quality improvement for flexible aircraft using multi-functional distributed flight control surfaces. A multi-objective optimal control design is developed to provide an acceleration suppression capability in conjunction with a gust load alleviation in order to provide ride quality improvement. A gust estimation is developed to estimate the gust load using a recursive least-squares algorithm. A ride quality assessment study is conducted using a flexible wing generic transport model. Six different flight control designs are implemented. The study shows that ride quality can be significantly improved with the acceleration suppression control.

I. Introduction

Air vehicles are typically designed to maintain sufficient structural rigidity for safe load-carrying capacity. Advanced composite materials have gained widespread adoption as materials of choice for modern airframe structures. This adoption is driven by the need to reduce airframe operational empty weight (OEW) which is a major consideration for improving energy efficiency. Composite structures tend to exhibit less structural rigidity while providing the same load-carrying capacity. As the wing flexibility increases, aeroelastic interactions can adversely affect aircraft performance and safe operation. Increased drag, hence increased fuel burn, is one such potential consequence. Without means for aeroelastic compensation, the benefit of weight reduction afforded by composite materials could be offset by reduced aerodynamic performance at off-design flight conditions. Another manifestation of increased wing flexibility is the adverse interaction with the stability and control of the aircraft. There is a greater degree of coupling between the elastic modes and the rigid-body modes of the aircraft as the structural stiffness of the wing decreases. This coupling could adversely impact the overall aircraft flight dynamic and control characteristics such as handling qualities, dynamic response during gust or wake encounters, and ride quality.

For passenger aircraft, ride quality is a measure of passenger comfort which is an important safety consideration. The dynamic response of a flexible aircraft during a gust or wake encounter comprises a rigid-body dynamic response component and a structural dynamic response component. The rigid-body dynamic response usually contains low frequency signals associated with the rigid-body modes which typically occur below 1 Hz for transport class aircraft. On the other hand, the structural dynamic response is generally associated with high frequency vibration of the wing structure under a continuous and discrete gust excitation. The excitation causes the elastic modes to respond in varying amounts at different frequencies. These elastic modes occur at a higher frequency range than the rigid-body modes. Passenger comfort is generally sensitive to high frequency vibratory motion than low frequency motion. Furthermore, the transmissibility of the gust load into the aircraft fuselage can excite the elastic modes of the fuselage and tails. The load transmission also causes the rigid-body modes to respond in concert with the elastic modes due to the coupling between these types of modes. Therefore, the high-frequency structural dynamic response can cause objectionable ride quality.

NASA had conducted extensive ride quality research in the 1970's and developed ride quality metrics to assess passenger comfort. One particular reference by Leatherwood, Dempsey, and Clevenson provides a design tool for estimating passenger ride discomfort.[1] They propose metrics for discomfort response to sinusoidal and random motions for a single axis and combined axes as a function of the frequencies of the dynamic response of the vehicle. They present a table of frequency ranges of stimulus values considered important for passenger ride discomfort. The study

*Senior Research Scientist and Technical Group Lead, Intelligent Systems Division, nhan.t.nguyen@nasa.gov
†Aerospace Engineer, Intelligent Systems Division, kelley.e.hashemi@nasa.gov

suggests that, for sinusoidal vibration, passenger ride discomfort falls with frequency ranges of 30 Hz for vertical motion, 10 Hz for lateral motion, and 4 Hz for roll motion. For random vibration, the frequency ranges of interest are 18 Hz for vertical motion and 10 Hz for lateral motion. Their study motivates the work in this paper which aims to address the structural dynamic response in the frequency ranges of stimulus values.

The objective of this study is to develop a flight control design that can improve the ride quality of a flexible wing transport aircraft. The aircraft model is the NASA Generic Transport Model (GTM) with flexible wings.[2] The rigid GTM has been used extensively in many flight control research. The flexible wing GTM has been developed as a research platform for development of performance adaptive aeroelastic wing (PAAW) technology for future high aspect ratio wing transports. The PAAW technology leverages multi-disciplinary solutions to maximize the aerodynamic performance payoff of future adaptive wing design, while addressing simultaneously operational constraints that can prevent the safe operation of those vehicles. These operational constraints include reduced flutter margins, increased dynamic responses to gust and maneuver loads, and degraded pilot handling qualities as well as ride quality. All of these constraints while seeking the optimal aerodynamic performance present themselves as a multi-objective flight control problem.[17]

A multi-objective flight control framework[4–8,17] has been developed to address these operational constraints and the efficiency goal simultaneously in order to arrive at optimal solutions that can provide good compromise between the efficiency goal and operational constraints. These optimal solutions take advantage of a distributed multi-functional flight control actuation concept developed by NASA called the Variable Camber Continuous Trailing Edge Flap (VCCTEF)[9,10,12,13] which can be used to simultaneously achieve multiple flight control objectives.

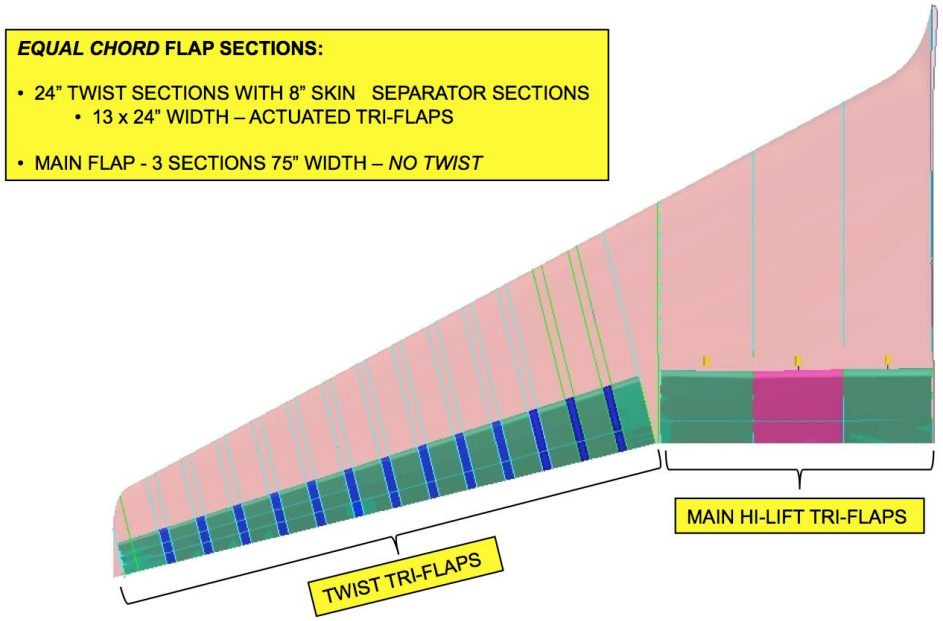

Figure 1. GTM with with Variable Camber Continuous Trailing Edge Flap

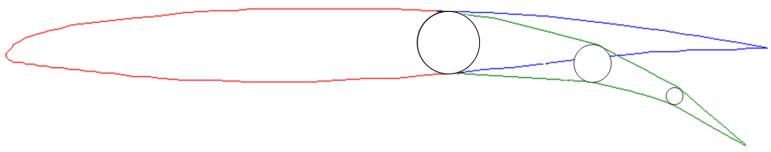

Figure 2. Three-Segment Variable Camber Flap

The VCCTEF concepts provide the ability to tailor the spanwise load or lift distribution via a continuous trailing edge formed by multiple spanwise flap sections which are joined together by elastomer transition sections as shown in Fig. 1. The spanwise load tailoring allows optimal lift distributions to be achieved throughout a given flight envelope, thereby enabling a mission-adaptive performance to reduce the fuel burn. The VCCTEF also provides the ability to tailor the chordwise pressure via a variable camber flap having multiple chordwise segments as shown in Fig. 2. These

chordwise flap segments can be individually commanded or actuated in unison when a flap deflection command is given. By varying the deflections of the individual chordwise flap segments, any aerodynamic surface can be created to achieve a desired aerodynamic performance.

II. Multi-Objective Flight Control

Fight control design of conventional aircraft has a long heritage with the single-axis flight control philosophy for pitch control by the elevator, roll control by the aileron, and yaw control by the rudder. The VCCTEF represents a new class of multi-functional flight control technology for future transport aircraft. This potentially could open up a new flight control paradigm. In the presence of multi-functional flight control surfaces such as the VCCTEF, a conventional flight control task such as a pitch command could be designed in conjunction with other flight control requirements particularly for flexible wing aircraft. These additional requirements may include: 1) drag minimization, 2) aeroelastic mode suppression, 3) maneuver load alleviation, 4) gust load alleviation. In addressing these requirements, the new flight control system would also address improvements in pilot handling qualities and passenger ride comfort.

To address all of these flight control objectives simultaneously can be a challenge in a flight control design. A multi-objective flight control framework can be developed to address the needs for satisfying multiple, competing flight control requirements. This paper will present a multi-objective adaptive control approach to address some of these multi-disciplinary interactions in a flexible wing aircraft employing a multi-functional flight control technology. A multi-objective flight control system has been previously developed to simultaneously gain aerodynamic efficiency, ASE mode suppression, and gust/maneuver load alleviation while maintaining traditional pilot command-tracking tasks for guidance and navigation.[4–8,17] This study continues to build upon the previous studies to address ride quality in the multi-objective flight control framework.

Figure 3 illustrates an architecture of a multi-objective flight control system. In addition, a real-time drag minimization control strategy is included in the guidance loop.[14,15] This feature utilizes system identification methods to estimate aerodynamic parameters for the on-line optimization. The aerodynamic parameters are also used in the multi-objective flight control for drag minimization and gust/maneuver load alleviation control.

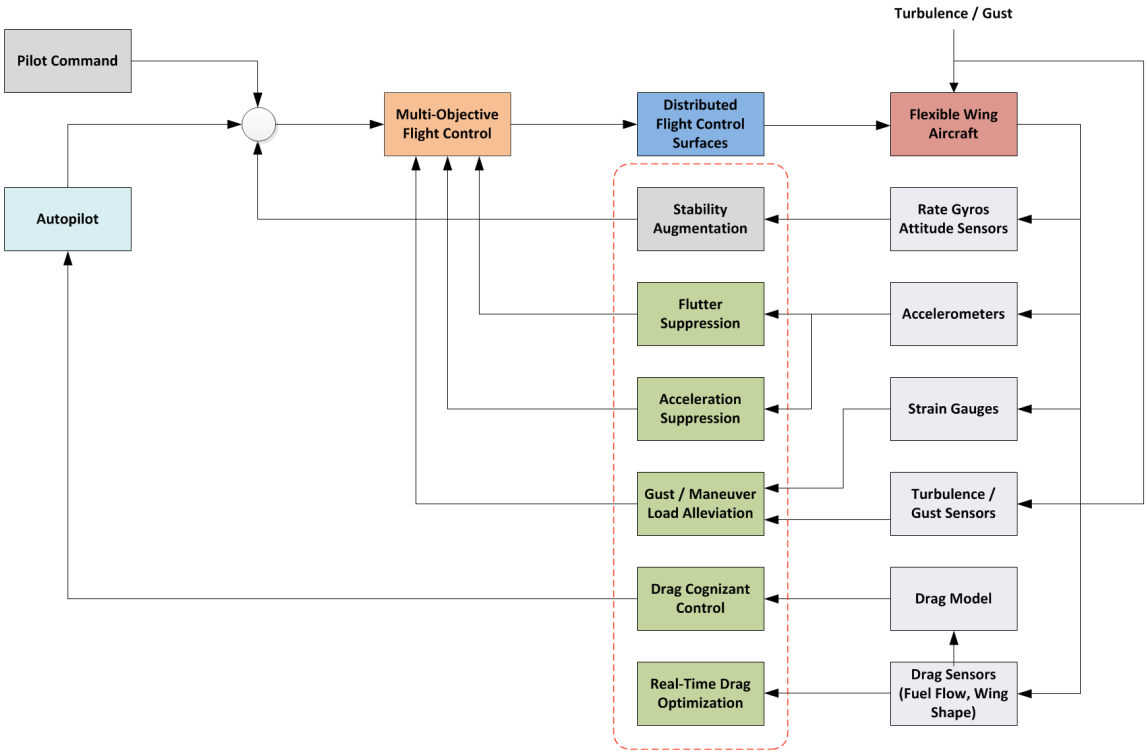

Figure 3. Multi-Objective Flight Control Architecture

The multi-objective flight control framework comprises the following objectives all acting in a synergistic manner:

1) traditional pilot command-following flight control, 2) drag minimization, 3) aeroelastic mode suppression, and 4) gust/maneuver load alleviation. Ride quality improvement objective can easily be incorporated in this framework by leveraging the aeroelastic mode suppression and gust load alleviation capabilities. In addition, a new acceleration suppression objective is also included. Each of these objectives can be a major flight control system design in its own right. Thus, a multi-objective flight control system can be a complex flight control design that takes into account multiple competing requirements to achieve optimal flight control solutions that strive to have a good balance among these requirements.

The flight dynamics of a flexible wing aircraft can be described in general by the following state-space equation:

$$\dot{x} = Ax + Bu + w \tag{1}$$

This equation can be separated in terms of the rigid-body and flexible dynamics

$$\begin{bmatrix} \dot{x}_r \\ \dot{x}_e \end{bmatrix} = \begin{bmatrix} A_{rr} & A_{re} \\ A_{er} & A_{ee} \end{bmatrix} \begin{bmatrix} x_r \\ x_e \end{bmatrix} + \begin{bmatrix} B_{rr} & B_{re} \\ B_{er} & B_{ee} \end{bmatrix} \begin{bmatrix} u_r \\ u_e \end{bmatrix} + \begin{bmatrix} w_r \\ w_e \end{bmatrix} \tag{2}$$

where $x_r(t)$ is rigid-body aircraft state vector which is available for feedback, $x_e(t)$ is the elastic state vector, $u_r(t)$ is the rigid-body aircraft control input vector comprising the conventional elevator, aileron, and rudder inputs, $u_e(t)$ represents the VCCTEF or any other types of control surface deflections on the aircraft wing, $w_r(t)$ represents the disturbance to the rigid-body states, and $w_e(t)$ represents the disturbance to the elastic states. For longitudinal dynamics, $u_r(t) = \delta_e(t)$ is the elevator control surface deflection and $u_e(t)$ are the symmetric VCCTEF control surface deflections. For lateral-directional dynamics, $u_r(t) = \begin{bmatrix} \delta_a(t) & \delta_r(t) \end{bmatrix}^\top$ are the aileron and rudder control surface deflections and $u_e(t)$ are the anti-symmetric VCCTEF control surface deflections.

The wing acceleration measurements are represented by

$$a = a_x x + a_u u + a_w w = \begin{bmatrix} a_{x_r} & a_{x_e} \end{bmatrix} \begin{bmatrix} x_r \\ x_e \end{bmatrix} + \begin{bmatrix} a_{u_r} & a_{u_e} \end{bmatrix} \begin{bmatrix} u_r \\ u_e \end{bmatrix} + \begin{bmatrix} a_{w_r} & a_{w_e} \end{bmatrix} \begin{bmatrix} w_r \\ w_e \end{bmatrix} \tag{3}$$

where $x(t) = \begin{bmatrix} x_r^\top(t) & x_e^\top(t) \end{bmatrix}^\top$, $u(t) = \begin{bmatrix} u_r^\top(t) & u_e^\top(t) \end{bmatrix}^\top$, and $w(t) = \begin{bmatrix} w_r^\top(t) & w_e^\top(t) \end{bmatrix}^\top$.

Collectively, the rigid-body aircraft states and wing acceleration measurements form the output of the system denoted by

$$y = Cx + Du + Ew = \begin{bmatrix} I & 0 \\ a_{x_r} & a_{x_e} \end{bmatrix} \begin{bmatrix} x_r \\ x_e \end{bmatrix} + \begin{bmatrix} 0 & 0 \\ a_{u_r} & A_{u_e} \end{bmatrix} \begin{bmatrix} u_r \\ u_e \end{bmatrix} + \begin{bmatrix} 0 & 0 \\ a_{w_r} & a_{w_e} \end{bmatrix} \begin{bmatrix} w_r \\ w_e \end{bmatrix} \tag{4}$$

where $y(t) = \begin{bmatrix} x_r^\top(t) & a^\top(t) \end{bmatrix}^\top$.

In addition, acceleration measurements on aircraft are available at selected locations for ride quality assessments such as, aircraft center of gravity (CG), tail location in the cabin, and the wing tip for roll and yaw. The aircraft acceleration vector expressed in the unit of g is given by

$$n = n_x x + n_u u + n_w w \tag{5}$$

The aircraft acceleration vector includes both translational acceleration components and angular acceleration components in the three aircraft body-fixed axes x, y, and z. The aforementioned reference suggests accelerations in the following five directions are particularly important for ride quality assessments for random vibration: vertical or the z-direction, lateral or the y-direction, longitudinal or the x-direction, roll, and pitch. For sinusoidal vibration, only the vertical, lateral, and roll directions are important.

The load response of aircraft during a gust encounter which can affect the ride quality includes the unsteady lift and the three unsteady moments in the roll, pitch, and yaw axes. The load transmission into the passenger cabin can create discomfort. The unsteady load response can be modeled by

$$P = P_x x + P_u u + P_w w \tag{6}$$

where P is a load vector which can be normalized by the aircraft weight for forces and by suitable moment references for moments.

Consider the structural dynamics of the flexible wing described by

$$\dot{x}_e = A_{ee}x_e + A_{er}x_r + B_e u_e + w_e \tag{7}$$

The structural dynamic response of the wing is influenced by the frequencies and damping values of the elastic modes of the wing. We can design a model-following controller to provide the desired frequency and damping characteristics of the elastic modes to suppress the structural dynamic response to a gust excitation. A reference model for the structural dynamics of the flexible wing can be formed as

$$\dot{x}_{e,m} = A_{ee,m}x_{e,m} + A_{er}x_r \tag{8}$$

where $A_{ee,m}$ provides the desired closed-loop frequency and damping characteristics of the elastic modes within the frequency range of interest.

The reference model of the structural dynamics of the flexible wing can be modeled as

$$M\ddot{u} + C\dot{u} + Ku = 0 \tag{9}$$

where M, C, and K are the mass, damping, and stiffness matrices of the wing structure; and $u(t)$ is a wing displacement vector.

To design the reference model for the structural dynamics of the flexible wing, we perform a modal coordinate transformation. Let $q(t) = \Phi^\top u(t)$ be a generalized displacement vector where Φ is a matrix of orthogonal eigenvectors of the matrix $M^{-1}K$. Then, we write the structural dynamic equation after premultiplying Eq. 9 by $\Phi^\top$ as

$$M_{gen}\ddot{q} + C_{gen}\dot{q} + K_{gen}q = 0 \tag{10}$$

where $M_{gen} = \Phi^\top M\Phi$, $C_{gen} = \Phi^\top C\Phi$, and $K_{gen} = \Phi^\top K\Phi$ are the generalized mass, damping, and stiffness matrices of the wing structure which are diagonal.

The frequency shaping can be designed by choosing the diagonal elements of the generalized damping matrix which can be written as

$$C_{gen} = \left\{2m_i\zeta_i\omega_i\delta_{ij}\right\}_{i,j=1}^{N} \tag{11}$$

where m_i, ζ_i, and ω_i are the generalized mass, damping, and frequency of the i-th flexible wing mode; and δ_{ij} is the Konecker delta.

Thus, the damping of the structural modes at the frequencies that affect the ride quality can be selected appropriately. Transforming back into the original coordinates yields

$$C = 2M\Phi\zeta\omega\Phi^\top \tag{12}$$

where $\zeta = \left\{\zeta_i\delta_{ij}\right\}_{i,j=1}^{N}$ and $\omega = \left\{\zeta_i\delta_{ij}\right\}_{i,j=1}^{N}$ are the diagonal damping ratio and frequency matrices.

The rigid-body aircraft dynamics which encapsulate the rigid-body dynamic response can also be shaped by a model-following controller. A reference model for the rigid-body aircraft dynamics can be established as

$$\dot{x}_{r,m} = A_{rr,m}x_{r,m} + A_{re}x_e + B_r K_r r \tag{13}$$

where $A_{rr,m}$ provides the desired closed-loop frequency and damping characteristics of the rigid-body aircraft modes to shape the aircraft handling qualities. If the flexible wing modes are well-damped by a suitable choice of the reference model for the structural dynamics, $x_e(t)$ would tend to zero and $x_r(t)$ would tend to the desired rigid-body states. The composite reference model must be stable which proper choices of $A_{rr,m}$ and $A_{ee,m}$. The entire reference model can be written as

$$\dot{x}_m = A_m x_m + B_m r \tag{14}$$

We formulate a multi-objective cost function as follows:

$$J = \lim_{t_f\to\infty}\frac{1}{2}\int_0^{t_f}\left[(x-x_m)^\top Q(x-x_m) + u^\top Ru + n^\top Q_n n + P^\top Q_P P\right]dt \tag{15}$$

where $Q = Q^\top > 0$, $Q_n = Q_n^\top > 0$, $Q_P = Q_P^\top > 0$, and $R = R^\top > 0$ are weighting matrices.

The third term in the cost function provides an acceleration suppression control feature. The fourth term is a gust load alleviation control feature.

The Hamiltonian is established as

$$H = \frac{1}{2}(x-x_m)^\top Q(x-x_m) + \frac{1}{2}u^\top Ru + \frac{1}{2}\left(x^\top n_x^\top + u^\top n_u^\top + w^\top n_w^\top\right) Q_n(n_x x + n_u u + n_w w) + \frac{1}{2}\left(x^\top P_x^\top + u^\top P_u^\top + w^\top P_w^\top\right) Q_P(P_x x + P_u u + P_w w) + \lambda^\top(Ax + Bu + w) \quad (16)$$

The necessary conditions for optimality are given by

$$\dot{\lambda} = -\frac{\partial H}{\partial x}^\top = -Q(x-x_m) - n_x^\top Q_n(n_x x + n_u u + n_w w) - P_x^\top Q_P(P_x x + P_u u + P_w w) - A^\top \lambda \quad (17)$$

$$\frac{\partial H}{\partial u}^\top = Ru + n_u^\top Q_n(n_x x + n_u u + n_w w) + P_u^\top Q_P(P_x x + P_u u + P_w w) + B^\top \lambda = 0 \quad (18)$$

The optimal control is then obtained as

$$u = -\left(R + n_u^\top Q_n n_u + P_u^\top Q_P P_u\right)^{-1}\left(B^\top \lambda + n_u^\top Q_n n_x x + n_u^\top Q_n n_w w + P_u^\top Q_P P_x x + P_u^\top Q_P P_w w\right) \quad (19)$$

Let $\lambda(t) = W(t)x(t) + V(t)$. Then, differentiating $\lambda(t)$ yields

$$\dot{W}x + W\bar{A}x + \bar{A}^\top Wx - WB\bar{R}^{-1}B^\top Wx + \bar{Q}x + \left(\bar{A}^\top - WB\bar{R}^{-1}B^\top\right)V + \dot{V} = Qx_m + Q_w w \quad (20)$$

where

$$\bar{R} = R + n_u^\top Q_n n_u + P_u^\top Q_P P_u \quad (21)$$

$$\bar{A} = A - B\bar{R}^{-1}\left(n_u^\top Q_n n_x + P_u^\top Q_P P_x\right) \quad (22)$$

$$\bar{Q} = Q + n_x^\top Q_n n_x + P_x^\top Q_P P_x - \left(n_x^\top Q_n n_u + P_x^\top Q_P P_u\right)\bar{R}^{-1}\left(n_u^\top Q_n n_x + P_u^\top Q_P P_x\right) \quad (23)$$

$$Q_w = \left(n_x^\top Q_n n_u + P_x^\top Q_P P_u + WB\right)\bar{R}^{-1}\left(n_u^\top Q_n n_w + P_u^\top Q_P P_w\right) - \left(n_x^\top Q_n n_w + P_x^\top Q_P P_w\right) - W \quad (24)$$

We choose Q_n and Q_P appropriately to ensure $\bar{Q} > 0$. For the infinite time-horizon optimal control, $\dot{W} = 0$ and $\dot{V} = 0$. Therefore, we obtain a modified Ricatti equation

$$W\bar{A} + \bar{A}^\top W - WB\bar{R}^{-1}B^\top W + \bar{Q} = 0 \quad (25)$$

and

$$V = \left(\bar{A}^\top - WB\bar{R}^{-1}B^\top\right)^{-1}(Qx_m + Q_w w) \quad (26)$$

The multi-objective optimal controller is expressed as

$$u = K_x x + K_m x_m + K_w w \quad (27)$$

where

$$K_x = -\bar{R}^{-1}\left(B^\top W + n_u^\top Q_n n_x + P_u^\top Q_P P_x\right) \quad (28)$$

$$K_m = -\bar{R}^{-1}B^\top\left(\bar{A}^\top - WB\bar{R}^{-1}B^\top\right)^{-1}Q$$

$$K_w = -\bar{R}^{-1}\left[B^\top\left(\bar{A}^\top - WB\bar{R}^{-1}B^\top\right)^{-1}Q_w + n_u^\top Q_n n_w + P_u^\top Q_P P_w\right] \quad (29)$$

Note that $x_e(t)$ is not available and therefore has to be estimated by a Luenberger observer design as

$$\dot{\hat{x}} = A\hat{x} + L(y - \hat{y}) + Bu + \hat{w} \quad (30)$$

where L is the Kalman filter observer gain.

The linear-quadratic Gaussian multi-objective control is then designed as

$$u = K_x\hat{x} + K_m x_m + K_w\hat{w} \quad (31)$$

Note that the multi-objective control would need the information on the disturbance estimate $\hat{w}(t)$. One approach is to use an extended state estimation where we represent the dynamics of the disturbance as

$$\dot{\hat{w}} = A_w \hat{w} \tag{32}$$

where A_w is a stable matrix.

Then, the extended state-space model is represented by

$$\dot{z} = A_z z + B_z u \tag{33}$$

where $z(t) = \begin{bmatrix} \hat{x}^\top(t) & \hat{w}^\top(x) \end{bmatrix}^\top$.

The output vector is expressed as in terms of the extended state vector as

$$y = C_z z + Du \tag{34}$$

Then, the extended-state estimation is designed by the Luenberger observer design as

$$\dot{z} = A_z z + L_z (y - \hat{y}) + B_z u \tag{35}$$

Then, the LQG multi-objective control is obtained as

$$u = K_z \hat{z} + K_m x_m \tag{36}$$

where $K_z = \begin{bmatrix} K_x^\top & K_w^\top \end{bmatrix}^\top$.

A more robust gust estimation is provided in the following section.

III. Gust Estimation

If the gust load acting on the rigid-body aircraft only has a vertical component in the plane of symmetry, then the elevator can be used to cancel out the pitching moment component of the gust load which is normally the greatest. The lift and drag components can be effectively canceled out using the flight control surfaces on the wings. Since it is assumed that there exist multiple distributed flight control surfaces, only two flight control surfaces are needed to cancel out the lift and drag components. Generally, lift is a much larger force than drag, so if drag is ignored, then only one flight control surface on the wing is required. For the gust load acting on the flexible wing, the most active ASE modes are identified and ranked based on their frequencies and damping values. Generally, only the first few lowest ASE modes are actively participating in the structural dynamic response. Sufficient control surface allocation can be designed to suppress the gust load components for these ASE modes.

Suppose $x_e(t)$ is ordered from most active ASE modes to the least active ASE modes based on the frequencies and damping values. It is assumed that the gust loads associated with the first n ASE modes are to be suppressed. The ASE state space model can be reduced in the order by a modal decomposition to retain only those active ASE modes. The higher frequency ASE modes which may not be controlled could be allowed to pass through provided their structural dynamic response characteristics are not significant.

Consider a symmetric vertical gust case, the rigid aircraft state vector is described by $x_r(t) = \begin{bmatrix} h(t) & V(t) & \alpha(t) & q(t) & \theta(t) & \beta(t) & p(t) & r(t) & \phi(t) \end{bmatrix}^\top$ where $h(t)$ is the altitude, $V(t)$ is the airspeed, $\alpha(t)$ is the angle of attack, $q(t)$ is the pitch rate, $\theta(t)$ is the pitch angle, $\beta(t)$ is the angle of sideslip, $p(t)$ is the roll rate, $r(t)$ is the yaw rate, and $\phi(t)$ is the bank angle. The gust load on the rigid aircraft is denoted as $w_r(t) = \begin{bmatrix} 0 & w_V(t) & w_\alpha(t) & w_q(t) & 0 & w_\beta(t) & w_p(t) & w_r(t) & 0 \end{bmatrix}^\top$. The aircraft acceleration measurements can be used to estimate the gust components due to the rigid-body aircraft motion. To estimate these gust load components, six acceleration measurements are required. This includes longitudinal, lateral, and vertical acceleration measurements in the x, y, and z directions at the aircraft CG denoted as $a_1(t)$, $a_2(t)$, and $a_3(t)$, a vertical acceleration measurement at a location on the left wing close to the side of body on the elastic axis denoted as $a_4(t)$, and vertical and lateral acceleration measurements in the tail on the centerline of the fuselage denoted as $a_5(t)$ and $a_6(t)$. The wing vertical acceleration $a_6(t)$ includes both the rigid-body vertical and roll accelerations as well as the vertical displacements of the elastic modes due to the bending and torsion motion of the wing. By placing the acceleration measurement $a_6(t)$ close to the side of the body, the contribution of the elastic modes should be small enough that the

rigid-body accelerations contribute mostly to the wing vertical acceleration. The relationship between the accelerations in the body-fixed axes and those in the stability axes are expressed as

$$\dot{u} = \dot{V}\cos\alpha\cos\beta - \dot{\alpha}V\sin\alpha\cos\beta - \dot{\beta}V\cos\alpha\sin\beta \tag{37}$$

$$\dot{v} = \dot{V}\sin\beta + \dot{\beta}V\cos\beta \tag{38}$$

$$\dot{w} = \dot{V}\sin\alpha\cos\beta + \dot{\alpha}V\cos\alpha\cos\beta - \dot{\beta}V\sin\alpha\sin\beta \tag{39}$$

Then, the mapping of these acceleration measurements is straight forwardly expressed as

$$a_r = \begin{bmatrix} a_1 \\ a_2 \\ a_3 \\ a_4 \\ a_5 \\ a_6 \end{bmatrix} = \begin{bmatrix} \dot{u} \\ \dot{v} \\ \dot{w} \\ \dot{w} + l_w\dot{p} \\ \dot{w} - l_t\dot{q} \\ \dot{v} - l_t\dot{r} \end{bmatrix} = \underbrace{\begin{bmatrix} \cos\alpha\cos\beta & -V\cos\alpha\sin\beta & -V\sin\alpha\cos\beta & 0 & 0 & 0 \\ \sin\beta & V\cos\beta & 0 & 0 & 0 & 0 \\ \sin\alpha\cos\beta & -V\sin\alpha\sin\beta & V\cos\alpha\cos\beta & 0 & 0 & 0 \\ \sin\alpha\cos\beta & -V\sin\alpha\sin\beta & V\cos\alpha\cos\beta & l_w & 0 & 0 \\ \sin\alpha\cos\beta & -V\sin\alpha\sin\beta & V\cos\alpha\cos\beta & 0 & -l_t & 0 \\ \sin\beta & V\cos\beta & 0 & 0 & 0 & -l_t \end{bmatrix}}_{G_r} \begin{bmatrix} \dot{V} \\ \dot{\beta} \\ \dot{\alpha} \\ \dot{p} \\ \dot{q} \\ \dot{r} \end{bmatrix} = G_r I_r \dot{x}_r \tag{40}$$

where l_w is the distance in the y-axis between the aircraft CG and the location of accelerometer $a_4(t)$, l_t is the distance in the x-axis between the aircraft CG and the locations of accelerometers $a_5(t)$ and $a_6(t)$ in the tail, and

$$I_r = \begin{bmatrix} 0 & 1 & 0 & 0 & 0 & 0 & 0 & 0 & 0 \\ 0 & 0 & 0 & 0 & 0 & 1 & 0 & 0 & 0 \\ 0 & 0 & 1 & 0 & 0 & 0 & 0 & 0 & 0 \\ 0 & 0 & 0 & 0 & 0 & 0 & 1 & 0 & 0 \\ 0 & 0 & 0 & 1 & 0 & 0 & 0 & 0 & 0 \\ 0 & 0 & 0 & 0 & 0 & 0 & 0 & 1 & 0 \end{bmatrix} \tag{41}$$

The estimated acceleration measurements can be expressed as

$$\hat{a}_r = G_r I_r \dot{\hat{x}}_r = G_r I_r \left(A_{rr}\hat{x}_r + A_{re}\hat{x}_e + B_{rr}u_r + B_{re}u_e\right) + G_r\hat{w}_1 \tag{42}$$

where $\hat{w}_1(t) = I_r\hat{w}_r(t) = \begin{bmatrix} w_V(t) & w_\alpha(t) & w_q(t) & w_\beta(t) & w_p(t) & w_r(t) \end{bmatrix}^\top$.

We formulate a cost function that minimizes the estimation error of the acceleration measurements

$$\min J = \frac{1}{2}\left(\hat{w}_1 - w_1\right)^\top\left(\hat{w}_1 - w_1\right) \tag{43}$$

We minimize the cost function by taking the partial derivative of J with respect to $\hat{w}_1(t)$

$$\frac{\partial J}{\partial \hat{w}_1^\top} = \left(\hat{w}_1 - w_1\right) \tag{44}$$

Let $\varepsilon_r(t) = \hat{a}_r(t) - a_r(t)$. Then, the cost function is expressed as

$$\frac{\partial J}{\partial \hat{w}_1^\top} = G_r^{-1}\varepsilon_r \tag{45}$$

We can formulate a recursive least-squares estimation as

$$\dot{\hat{w}}_1 = -\Gamma_r\left(G_r^{-1}\varepsilon_r + \sigma_r\hat{w}_1\right) \tag{46}$$

$$\dot{\Gamma}_r = -\mu_r\Gamma_r G_r^{-1} G_r^{-\top}\Gamma_r \tag{47}$$

where $\Gamma_r = \Gamma_r^\top > 0$ is a learning rate matrix, and $\sigma_r > 0$ and $\mu > 0$ are parameters to improve robustness.

This estimation can be shown to be stable.

To estimate the gust load on the flexible wing, suppose we use n_a acceleration measurements on the wing including $a_6(t)$ and $n_a < n_e$ where n_e is the number of structural dynamic modes in the state-space model. Then, we write

$$\hat{a}_e = a_{x_r}\hat{x}_r + a_{x_e}\hat{x}_e + a_u u + a_w \hat{w}_r + a_{w_e}\hat{w}_2 \tag{48}$$

where $\hat{w}_2(t) = I_e \hat{w}_e(t)$ is the non-zero elements of $\hat{w}_e(t)$.

The matrix a_{w_e} is of the size $n_a \times n_{w_2}$ where $n_a < n_{w_2}$ and n_{w_2} is the number of non-zero elements of $w_e(t)$. Then, minimizing the cost function

$$\min J = \frac{1}{2}(\hat{w}_2 - w_2)^\top (\hat{w}_2 - w_2) \tag{49}$$

yields a recursive least-squares estimation of $\hat{w}_2(t)$ as

$$\dot{\hat{w}}_2 = -\Gamma_e \left[a_{w_e}^\top \left(a_{w_e} a_{w_e}^\top \right)^{-1} \varepsilon_e + \sigma_e \hat{w}_2 \right] \tag{50}$$

$$\dot{\Gamma}_e = -\mu_e \Gamma_e a_{w_e}^\top \left(a_{w_e} a_{w_e}^\top \right)^{-1} \left(a_{w_e} a_{w_e}^\top \right)^{-\top} a_{w_e} \Gamma_e \tag{51}$$

where $\varepsilon_e(t) = \hat{a}_e(t) - a_e(t)$.

It should be noted that if $\mu_r = 0$ and $\mu_e = 0$ and if the output vector comprises all the acceleration measurements. Let $y(t) = \begin{bmatrix} a_r^\top(t) & a_e^\top(t) \end{bmatrix}^\top$. Then, the least-squares estimation is linear and can be expressed as

$$\dot{\hat{w}} = -\Gamma(\hat{y} - y) - \Lambda \hat{w} = -(\Gamma E + \Lambda)\hat{w} - \Gamma C(\hat{x} - x) + \Gamma E w \tag{52}$$

where

$$\Gamma = \begin{bmatrix} I_r^\top \Gamma_r G_r^{-1} & 0 \\ 0 & I_e^\top \Gamma_e a_{w_e}^\top \left(a_{w_e} a_{w_e}^\top \right)^{-1} \end{bmatrix} \tag{53}$$

$$\Lambda = \begin{bmatrix} \sigma_r I_r^\top \Gamma_r I_r & 0 \\ 0 & \sigma_e I_e^\top \Gamma_e I_e \end{bmatrix} > 0 \tag{54}$$

The stability of the gust estimation can be established by ensuring $\Re(\lambda(\Gamma E + \Lambda)) > 0$. In addition, the stability of the combined system including the plant and the state estimation can also be examined together with the least-squares estimation.

IV. Simulations

A. Aircraft Model

The GTM[16] represents a notional single-aisle, mid-size, 200-passenger transport aircraft generically approximating a Boeing 757 configuration, as shown in Fig. 4. The aircraft has a mid-cruise weight of 210,000 lbs for a typical operating load (gear up, flap up) that includes cargo, fuel, and passengers. Fuel weighs about 50,000 lbs for a range of about 3,000 nautical miles. At the design cruise condition of Mach 0.797 at 36,000 ft, the design lift coefficient is 0.51.

The GTM had been extensively tested in the 14-foot–by-22-foot wind tunnel at NASA Langley Research Center. Thus, wind tunnel test data are available for validation of computational models. A flight dynamic model of the rigid GTM with damaged aerodynamic surfaces was developed in 2006. This model has been used extensively in flight control research.[17,18]

A flexible wing GTM flight dynamic model has been developed as a research platform for the development of advanced adaptive wing control technologies for future transport aircraft.[2] The structural stiffness of the flexible wing is scaled down by a factor of two from the baseline wing stiffness as provided by Boeing. The resulting increase in the wing flexibility represents a typical structural flexibility of modern high aspect ratio wing transport aircraft.

The flight dynamic model of the rigid GTM is coupled to an aeroservoelastic (ASE) finite-element model (FEM) of the wing structure. The FEM computes the mode shapes and displacements of the wing structure. The coupled ASE-flight dynamic model is evaluated for Mach 0.8 and an altitude of 36,000 ft with 80% fuel loading. Figures 5 and 6 show the ASE pole locations of the first 198 symmetric and anti-symmetric modes of the flexible wing GTM.

All the ASE poles are stable at this flight condition. Table 1 shows the eigenvalues of the ASE coupled and uncoupled rigid-body aircraft modes of the GTM. The ASE coupling does significantly alter the rigid-body aircraft modes.

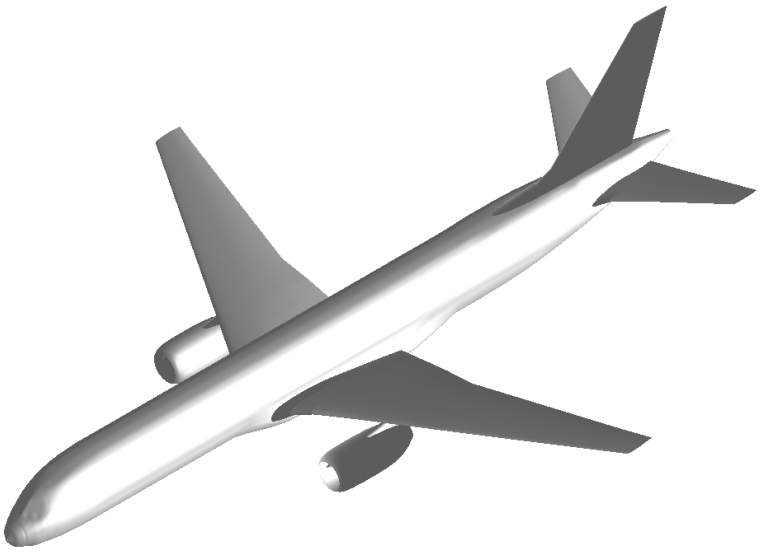

Figure 4. NASA Generic Transport Model

Rigid-Body Mode	ASE Coupled Eigenvalues	Uncoupled Eigenvalues
Phugoid	$-0.0064 \pm 0.0837i$	$-0.0047 \pm 0.0828i$
Short Period	$-0.5328 \pm 1.6576i$	$-0.5071 \pm 1.3590i$
Dutch-Roll	$-0.2939 \pm 1.5059i$	$-0.2663 \pm 1.5492i$
Roll	-1.0472	-1.0845
Spiral	-0.0202	-0.0219

Table 1. Eigenvalues of ASE Coupled and Uncoupled Rigid-Body Modes of the Flexible Wing GTM

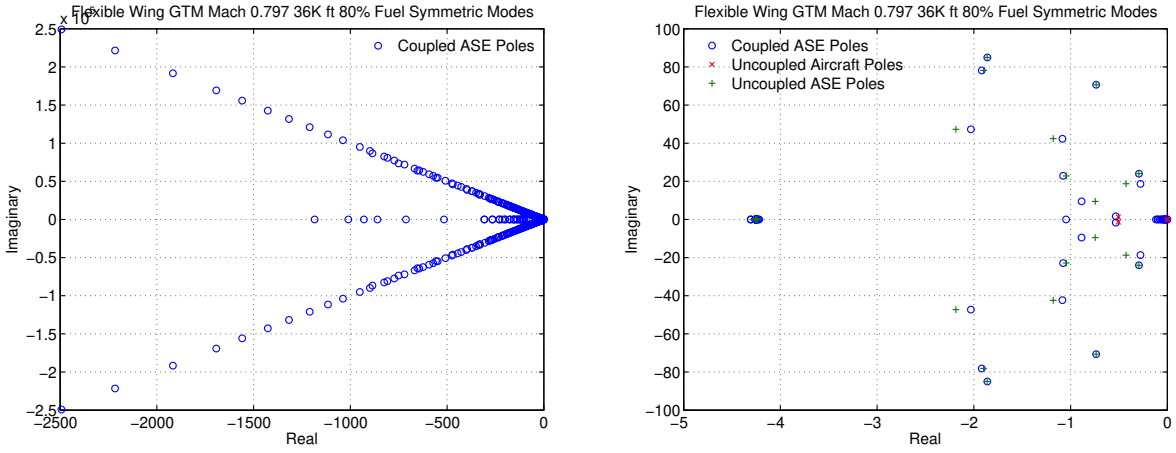

Figure 5. Pole Locations of Symmetric Modes of Flexible Wing GTM

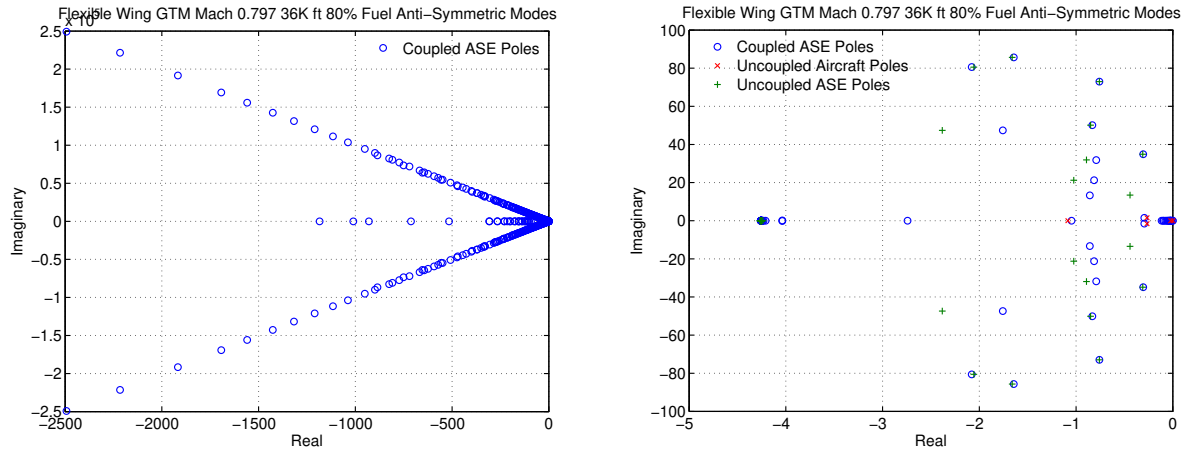

Figure 6. Pole Locations of Anti-Symmetric Modes of Flexible Wing GTM

A model reduction is performed to retain only the first ten ASE modes up to about 20 Hz. This frequency range is considered relevant for ride discomfort assessment for random vibration in the vertical plane.[1] Table 2 shows the eigenvalues of the first ten symmetric and anti-symmetric ASE modes of the flexible GTM wing. The fundamental frequency of the first bending symmetric ASE mode is 9.4109 rad/sec or 1.4978 Hz. The fundamental frequency of the first bending anti-symmetric ASE mode is 13.2072 rad/sec or 2.1020 Hz. A flutter analysis is conducted and shows that the first flutter mode is associated with the second bending symmetric ASE mode which occurs at Mach 0.958 corresponding to a flutter frequency of 17.8167 rad/sec or 2.8356 Hz.[19]

ASE Mode	Symmetric ASE Mode Eigenvalues	Symmetric Structural Dynamic Mode Eigenvalues	Anti-Symmetric ASE Mode Eigenvalues	Anti-Symmetric Structural Dynamic Mode Eigenvalues
1	$-0.8426 \pm 9.3731i$	$-0.0729 \pm 7.2936i$	$-0.8009 \pm 13.1829i$	$-0.1116 \pm 11.1569i$
2	$-0.2818 \pm 18.6759i$	$-0.1907 \pm 19.0694i$	$-0.7932 \pm 21.2460i$	$-0.2107 \pm 21.0691i$
3	$-1.0351 \pm 22.8182i$	$-0.2153 \pm 21.5297i$	$-0.7716 \pm 31.7682i$	$-0.3117 \pm 31.1694i$
4	$-0.2903 \pm 24.0005i$	$-0.2401 \pm 24.0042i$	$-0.3090 \pm 34.8691i$	$-0.3485 \pm 34.8473i$
5	$-1.0543 \pm 42.3144i$	$-0.4192 \pm 41.9200i$	$-1.7224 \pm 47.5924i$	$-0.4991 \pm 49.9050i$
6	$-1.9655 \pm 47.5078i$	$-0.5160 \pm 51.5980i$	$-0.8172 \pm 50.1101i$	$-0.5174 \pm 51.7423i$
7	$-0.7339 \pm 70.6620i$	$-0.7065 \pm 70.6513i$	$-0.7575 \pm 72.9492i$	$-0.7294 \pm 72.9370i$
8	$-1.8622 \pm 78.2028i$	$-0.7900 \pm 78.9950i$	$-2.0143 \pm 80.6593i$	$-0.8188 \pm 81.8763i$
9	$-1.8256 \pm 85.0657i$	$-0.8735 \pm 87.3478i$	$-1.6216 \pm 85.7461i$	$-0.8760 \pm 87.5923i$
10	$-2.3754 \pm 122.32i$	$-1.2318 \pm 123.17i$	$-2.3030 \pm 128.34i$	$-1.2332 \pm 123.31i$

Table 2. Eigenvalues of ASE and Structural Dynamic Modes of the Flexible Wing GTM

A coupled ASE longitudinal flight dynamic model of the flexible wing GTM is used for this study.[?] The model has 5 rigid aircraft states in the longitudinal direction but the airspeed and altitude states are removed, 10 aeroelastic modes with 2 elastic states and 4 aerodynamic lag states per mode, two rigid aircraft flight control inputs; namely, the elevator and engine throttle but the engine throttle is removed, and 16 VCCTEF inputs to the outermost chordwise flap segments. Thus, the model has a total of 63 states and 17 control variables. Due to the stiffness imposed by the elastomer transition section, a constraint on the relative deflection of any two adjacent flaps is imposed on the control input command. In order to address this relative deflection constraint, a virtual control concept is used whereby the VCCTEF deflection is mapped into a mathematically smooth shape function whose coefficients are the virtual control variables.[?] A cubic Chebyshev polynomial is selected as a candidate shape function. Then, the flap deflection of the

i-th flap is expressed as

$$\delta_i = c_0 + c_1 k + c_2\left(2k^2 - 1\right) + c_3\left(4k^3 - 3k\right) \tag{55}$$

where $k = \frac{i-1}{n-1}$, $i = 1,2,\ldots,16$, $n = 16$ with δ_1 being the inboard flap, and $c_j(t)$, $j = 0,1,2,3$ are the virtual control variables. Thus, the flexible wing control vector is represented by $u_e(t) = \begin{bmatrix} c_0(t) & c_1(t) & c_2(t) & c_3(t) \end{bmatrix}^\top$.

Figure 7 illustrates an acceleration sensor configuration that forms a minimum set of acceleration sensors for ride quality assessments in the vertical plane. Two accelerometers are placed in pair at the wing tip. One accelerometer is placed forward of the elastic axis and one is placed aft of the elastic axis. The accelerometer locations on the left wing are indicated by the two red dots in Fig. 7.[?] By placing the accelerometers in pair forward and aft of the elastic axis, it is possible to not only measure the vertical acceleration of the wing section, but also the angular acceleration, i.e., twist acceleration. At a minimum, the two wing tip accelerometers suffice for a flight control design. Care must be exercised in the accelerometer signal conditioning to ensure synchronous sampling to prevent a phase shift among the accelerometer signals which could affect the control objective. Two normal acceleration measurements are available from two accelerometers placed on the fuselage center line at the aircraft CG corresponding to accelerometer $a_3(t)$ and at a location 70 ft behind the aircraft CG near the quarter chord of the mean aerodynamic chord of the horizontal tail corresponding to accelerometer $a_5(t)$, as shown in Fig. 7. Additionally, a strain gauge sensor is placed in the proximity of the wing root on a load carrying member of the wing box. The strain gauge can be calibrated as a function of known static wing bending loads to provide a calibration relationship for estimating the wing lift in flight.

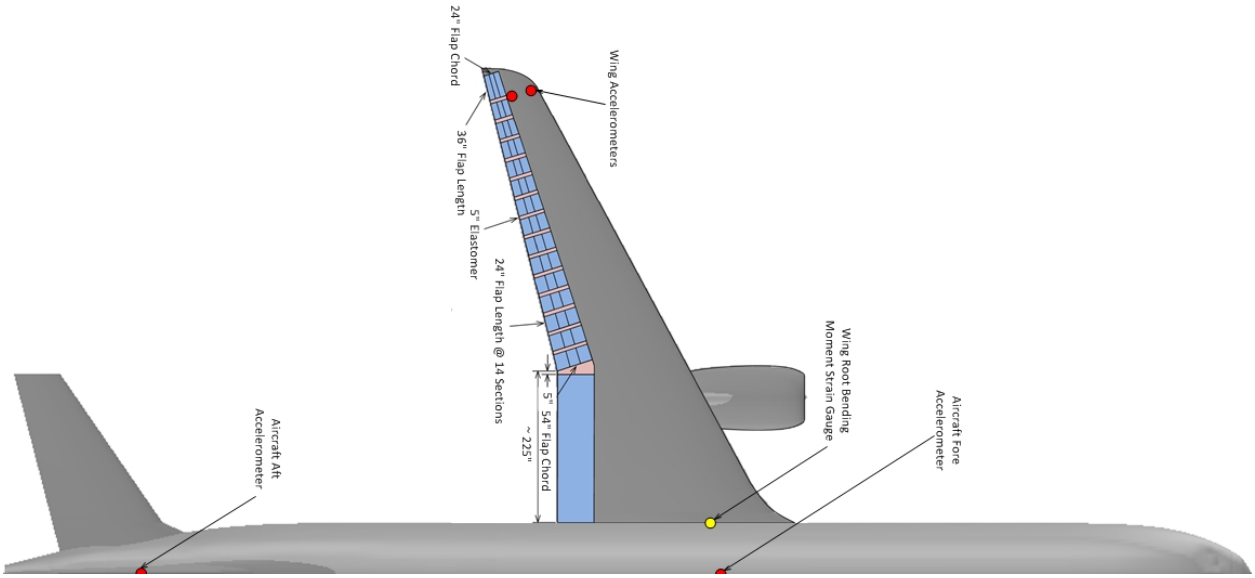

Figure 7. Acceleration Sensors for Ride Quality Assessments

A Von Karman turbulence continuous gust model is used in the simulation. The response of the vertical gust velocity to a random input is modeled by the transfer function $H(\omega)$

$$\frac{w_g}{w_{in}} = H(\omega) = \sigma\sqrt{\frac{L}{V}}\,\frac{1 + 2.7478\frac{L}{V}s + 0.3398\frac{L^2}{V^2}s^2}{1 + 2.9958\frac{L}{V}s + 1.9754\frac{L^2}{V^2}s^2 + 0.1539\frac{L^3}{V^3}s^3} \tag{56}$$

where σ is the turbulence intensity, L is the characteristic length, V is the airspeed, and ω is the frequency of the spectrum.

The turbulence intensity at low altitudes is given by $\sigma = 0.1 w_{20}$ where w_{20} is the wind speed at an altitude of 20 ft and is equal to 15 knots or 25.3 ft/sec for light turbulence, 30 knots or 50.6 ft/sec for moderate turbulence, and 45 knots or 76.0 ft/sec for severe turbulence. At high altitudes, the turbulence intensity is given by a table look-up. The characteristic length above 2000 ft is equal to $L = 2500$ ft based on MIL-F-8785C. A severe turbulence with the turbulence intensity of $\sigma = 18$ ft/s at 36,000 ft is selected for the simulations to challenge the ride quality flight control design.

B. Flight Control Simulations

A flight path angle controller is designed for the reference model to maintain a wing-level flight with zero flight path angle γ. The flight path angle control is labeled as γ control. The state weighting matrix is selected to be $Q = \text{diag}\,(Q_r, Q_e)$ where $Q_r = F^\top q_r F$ with $F = \begin{bmatrix} -1 & 0 & 1 \end{bmatrix}$ and $q_r = 1$ and $Q_e = I$. The acceleration weighting matrix is selected to be $Q_n = 100I$. The load weighting matrix is selected to be $Q_P = 100$. The control weighting matrix is selected to be $R = 1000I$.

The output vector are the four accelerometers. The accelerometers are modeled with a Gaussian white noise having a root mean squares (RMS) amplitude of $\sqrt{2}$ ft/s^2. A Kalman filter design is implemented with the observer weighting matrices selected to be $Q_{obs} = 10I$ and $R_{obs} = 100I$. Six different flight control designs and simulations are conducted. When Q_n is non-zero, the flight control is referred to as an acceleration suppression (AS) control. When Q_P is non-zero, the flight control is called a gust load alleviation (GLA) control. Gust disturbance estimation is implemented using the recursive least-squares algorithms in all but one simulations.

Flight Control Design	γ Control	AS Control	GLA Control	Gust Estimation	VCCTEF
1	On	Off	Off	On	On
2	On	Off	Off	On	Off
3	On	$Q_n = 100$	Off	On	On
4	On	$Q_n = 100$	$Q_P = 100$	On	On
5	On	$Q_n = 100$	$Q_P = 1000$	On	On
6	On	$Q_n = 100$	$Q_P = 100$	Off	On

Table 3. Flight Control Designs and Simulations

1. Flight Control Design 1: Flight Path Angle Control with Elevator and VCCTEF

The simulations are conducted first with the flight path angle control alone by setting $Q_n = 0$ and $Q_P = 0$. Figures 8(a) and 8(b) are the plots of the angle of attack and the modal velocity of the third elastic mode which is the most active. Note that the angle of attack varies rapidly from about 1.8° to -1.2° about the trim angle of attack, indicating a severe turbulence. Figures 9(a) and 9(b) show the rigid-body vertical accelerations N_z inside the aircraft fuselage at the CG and the tail and the vertical accelerations at the wing tip. Note that rigid-body accelerations swing from about 1.1 g's to -1.8 g's about the 1-g trim at 6 seconds where the aircraft experiences a negative-g plunge. The vertical accelerations N_z at the wing tip are almost at ± 40 g's, indicating a large-amplitude motion at the wing tip. Figure 10(a) and 10(b) show the control surface deflections of the elevator and the 16 trailing edge elements of the VCCTEF.

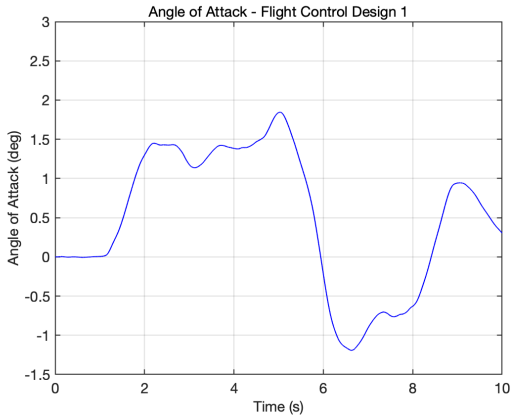

(a) Angle of Attack

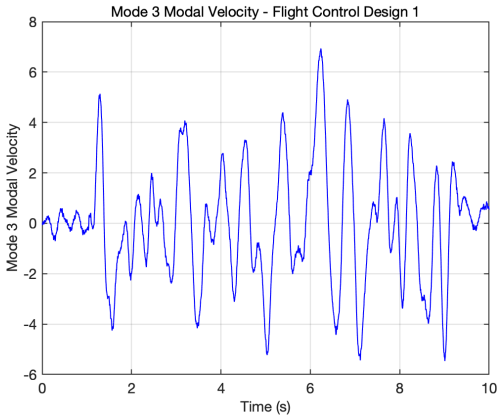

(b) Mode 1 Modal Velocity

Figure 8. Angle of Attack and Modal Velocity - Flight Control Design 1

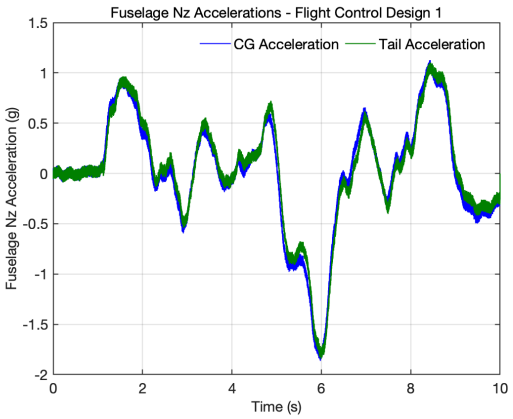

(a) Fuselage Vertical Accelerations

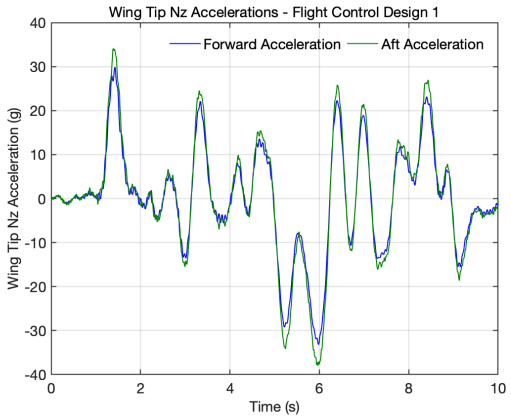

(b) Wing Tip Vertical Accelerations

Figure 9. Fuselage and Wing Tip Vertical Accelerations - Flight Control Design 1

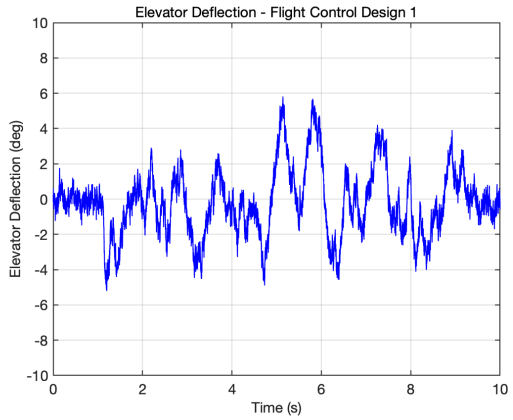

(a) Elevator Deflection

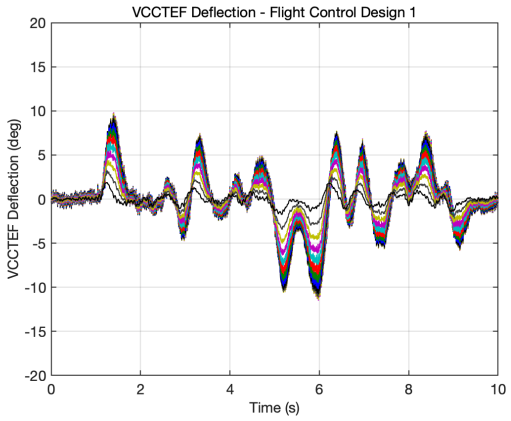

(b) VCCTEF Deflections

Figure 10. Control Surface Deflections - Flight Control Design 1

2. *Flight Control Design 2: Flight Path Angle Control with Elevator Only*

In the simulation above, the control surfaces of the VCCTEF on the wing are deployed. One possible explanation for the large amplitudes of the wing tip accelerations is that the control surfaces of the VCCTEF are commanded in such a way that they generate an excitation of the wing ASE modes, thereby causing large-amplitude motion of the wing. The flight path angle control has no objective in suppressing the vertical accelerations but the design includes the modal suppression objective via the weighting matrix $Q_e = I$. To illustrate this explanation, a simulation is conducted with the standard pitch-axis flight control system using only the elevator. Figure 11(a) shows the angle of attack which slightly decreases over that with the VCCTEF active. The modal velocity of the third mode decreases substantially as seen in Fig. 11(b). The fuselage vertical accelerations slightly decrease as shown in Fig. 12(a). The wing tip vertical accelerations also substantially decrease to about ± 2.8 g's as compared to about ± 40 g's when the control surfaces of the VCCTEF are deployed. The elevator deflection is shown in Fig. 13.

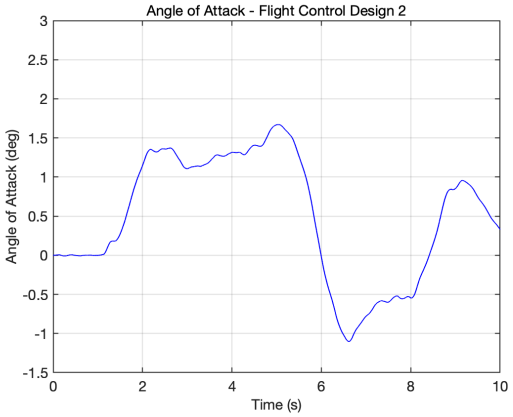

(a) Angle of Attack

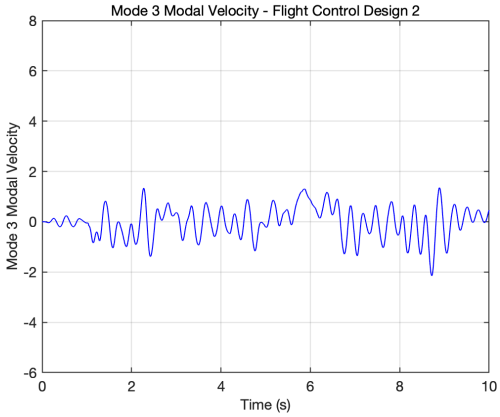

(b) Mode 1 Modal Velocity

Figure 11. Angle of Attack and Modal Velocity - Flight Control Design 2

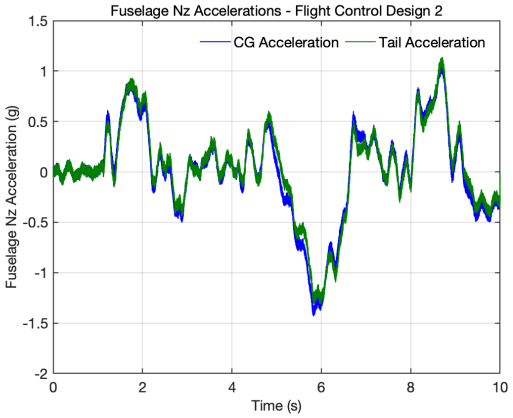

(a) Fuselage Vertical Accelerations

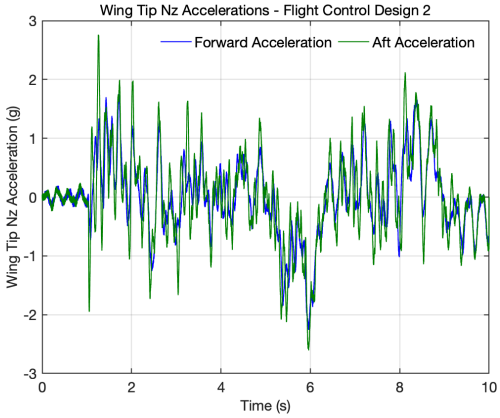

(b) Wing Tip Vertical Accelerations

Figure 12. Fuselage and Wing Tip Vertical Accelerations - Flight Control Design 2

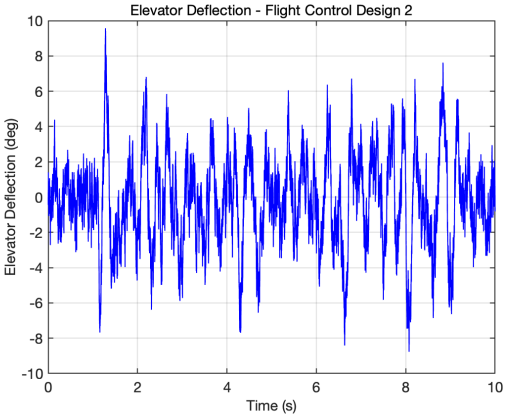

(a) Elevator Deflection

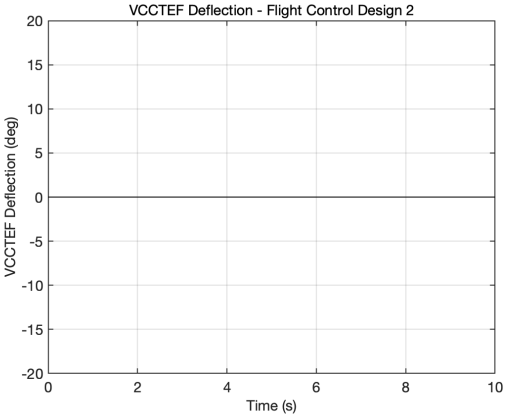

(b) VCCTEF Deflections

Figure 13. Control Surface Deflections - Flight Control Design 2

3. *Flight Control Design 3: Flight Path Angle - Acceleration Suppression Control*

The acceleration suppression control is turned on next with $Q_n = 100I$. The results show a dramatic decrease in the vertical acceleration levels across the board when comparing to both flight control designs 1 and 2. Figures 14(a) shows a decreases in the amplitude of the angle of attack which is now between 1.4° and -0.2°. The reduction in the negative angle of attack results in a decrease in the negative fuselage vertical acceleration to within 0.5 g to -0.8 g as seen in 15 Fig. (a). Figure 14(b) shows the modal velocity of the third mode which is about double that of flight control design 2. A dramatic decrease in the wing tip vertical acceleration is seen in Fig. 15(b). Comparing to flight control design 1, the decrease is about 20 times. Comparing to flight control design 2, the decrease is about 2.5 times. Figures 16(a) and 16(b) show the control surface deflections. The control surfaces of the VCCTEF are much more active than those with the flight control design 1. The simulation thus demonstrates the effectiveness of the acceleration suppression control in the multi-objective control framework.

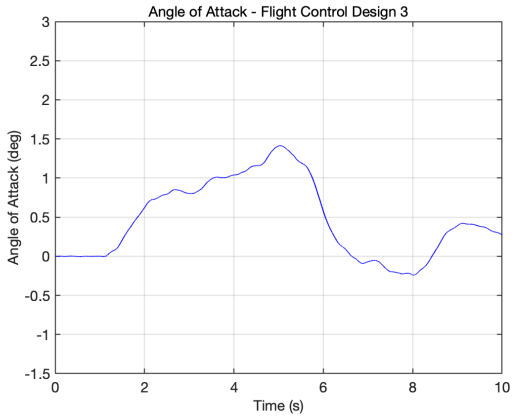

(a) Angle of Attack

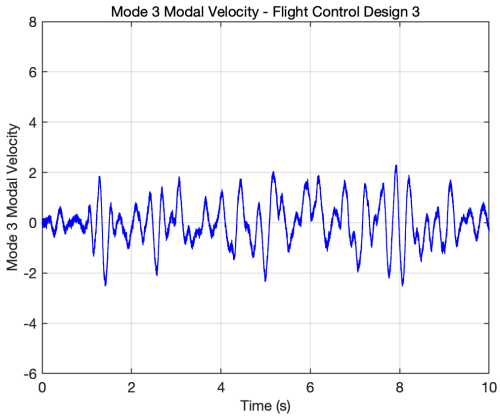

(b) Mode 1 Modal Velocity

Figure 14. Angle of Attack and Modal Velocity - Flight Control Design 3

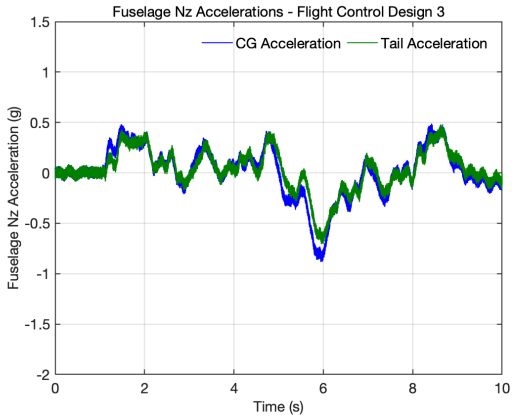

(a) Fuselage Vertical Accelerations

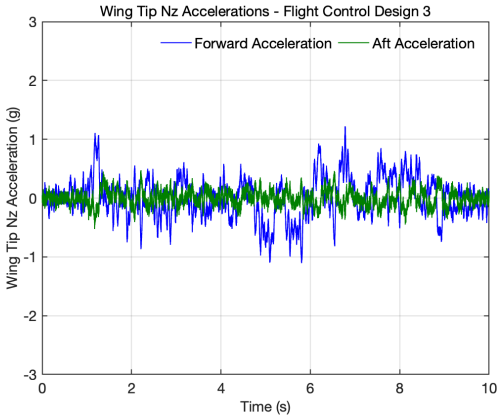

(b) Wing Tip Vertical Accelerations

Figure 15. Fuselage and Wing Tip Vertical Accelerations - Flight Control Design 3

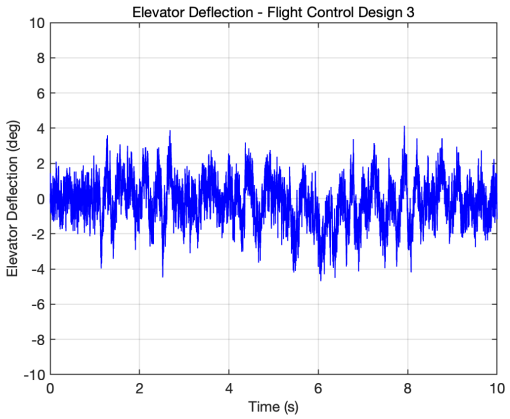

(a) Elevator Deflection

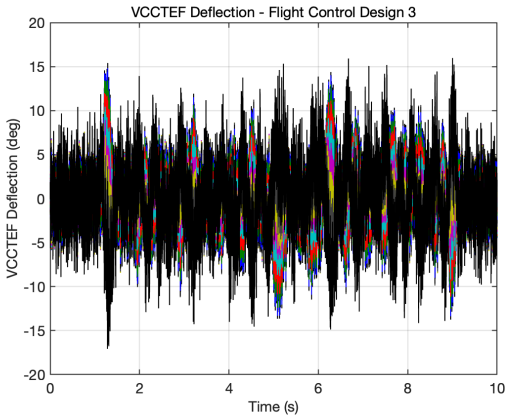

(b) VCCTEF Deflections

Figure 16. Control Surface Deflections - Flight Control Design 3

4. Flight Control Design 4: Flight Path Angle - Acceleration Suppression - Gust Load Alleviation Control

The gust load alleviation control is turned on next with $Q_P = 100I$. The flight control system now has three objectives working synergistically to maintain a wing-level flight, suppress the vertical accelerations, and alleviate the gust loads acting on the aircraft structure. Figures 17 (a) and 17 (b) show the angle of attack and modal velocity of the third mode. The angle of attack increases somewhat over that with flight control design 3. The modal velocity of the third mode maintains a similar amplitude as that with flight control design 3. This suggests that the gust load alleviation control does not contribute much to the modal suppression of the wing structure. The fuselage and wing tip vertical accelerations are shown in Figs. 18(a) and 18(b). The fuselage vertical accelerations have larger amplitudes than those with flight control design 3. The control surface deflections are shown in Figs. 19(a) and 19(b).

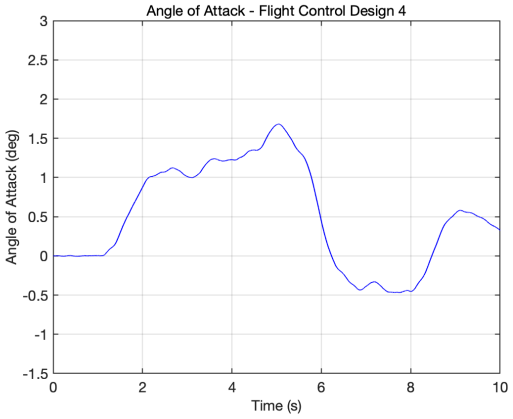

(a) Angle of Attack

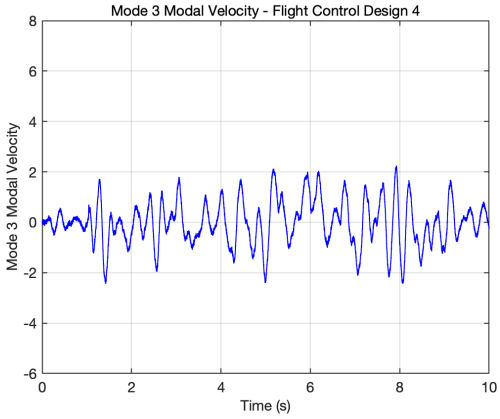

(b) Mode 1 Modal Velocity

Figure 17. Angle of Attack and Modal Velocity - Flight Control Design 4

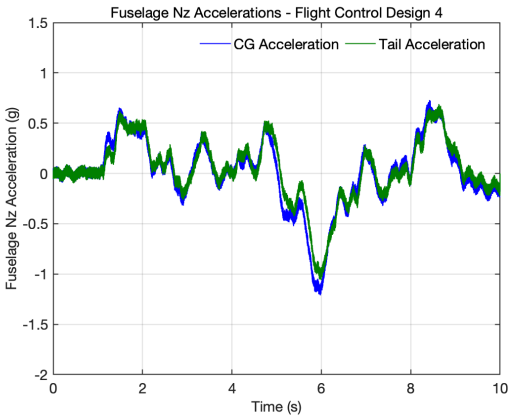

(a) Aircraft Fuselage Vertical Accelerations

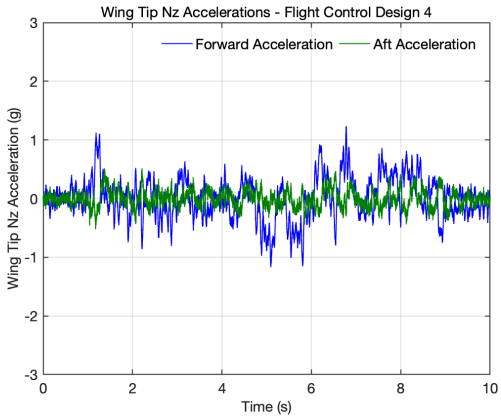

(b) Wing Tip Vertical Accelerations

Figure 18. Aircraft Fuselage and Wing Tip Vertical Accelerations - Flight Control Design 4

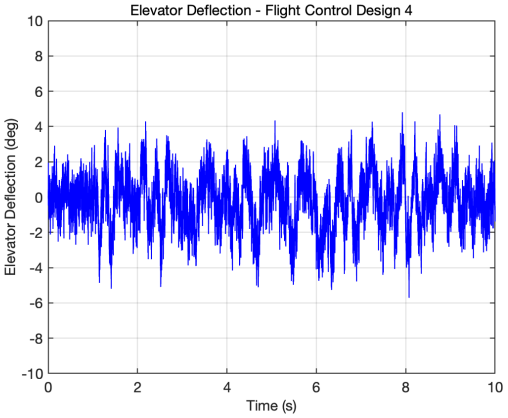

(a) Elevator Deflection

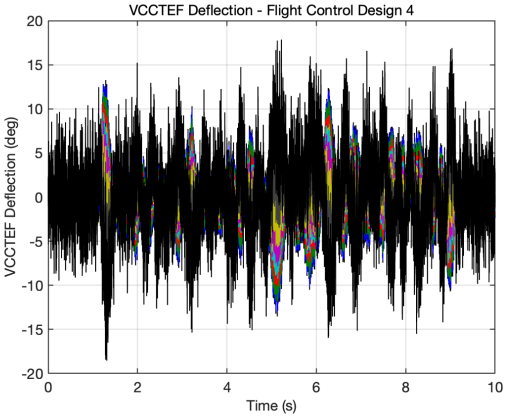

(b) VCCTEF Deflections

Figure 19. Control Surface Deflections - Flight Control Design 4

5. Flight Control Design 5: Flight Path Angle - Acceleration Suppression - Gust Load Alleviation Control with Higher Weighting for Gust Load Alleviation

In general, the gust load alleviation control does not seem to show a significant improvement over the acceleration suppression control. However, this could be due to the selection of the weighting matrix of $Q_p = 100I$. To examine this effect, flight control design 5 is simulated with $Q_P = 1000I$. Figures 20(a)-20(d) show the load factors for flight control designs 2-5. By definition, the load factor is the ratio of lift to weight of an aircraft. The acceleration suppression control causes the alternating component of the load factor to significantly increase as seen in Fig. 20 (b) when comparing to the load factor with flight control design 1. The gust load alleviation control with $Q_P = 100$ is seen to reduce substantially the alternating component of the load factor due to the acceleration suppression control. Increasing Q_P to 1000 further removes the high-frequency content in the load factor, but the load factor with flight control design 5 is essentially about the same in amplitude and characteristics as that with flight control design 2. I can be seen that there is a trade-off between the acceleration suppression and gust load alleviation. Increasing Q_P causes the vertical accelerations to increase as seen with flight control designs 3 and 4, but at the same time reduces the load factor. Thus, these competing objectives should be addressed in Pareto optimal sense. In general, some degree of gust load alleviation is necessary for ride quality. The high-frequency load factor associated with the acceleration suppression control alone can excite cabin interior structures and can cause ride discomfort, notwithstanding the structural integrity aspect.

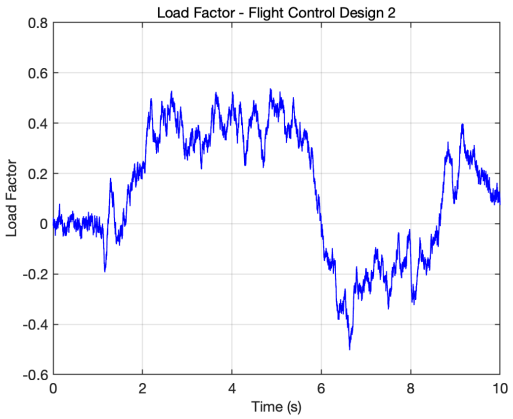

(a) Load Factor - Flight Control Design 2

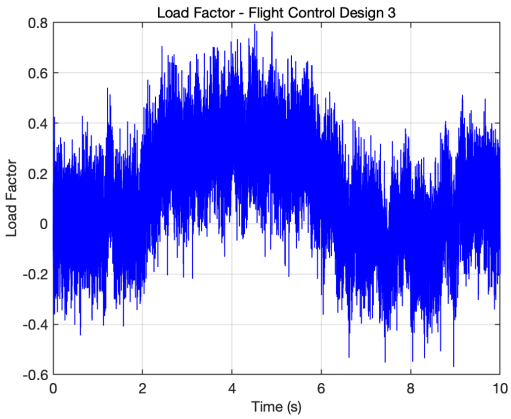

(b) Load Factor - Flight Control Design 3

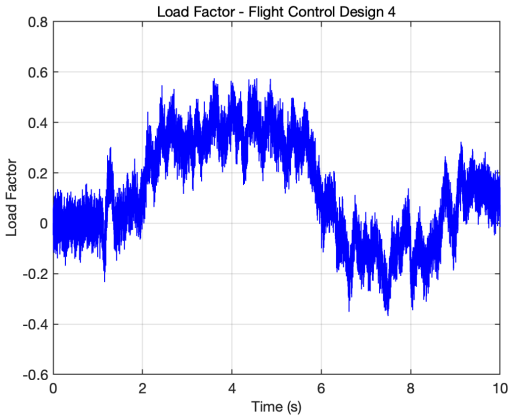

(c) Load Factor - Flight Control Design 4

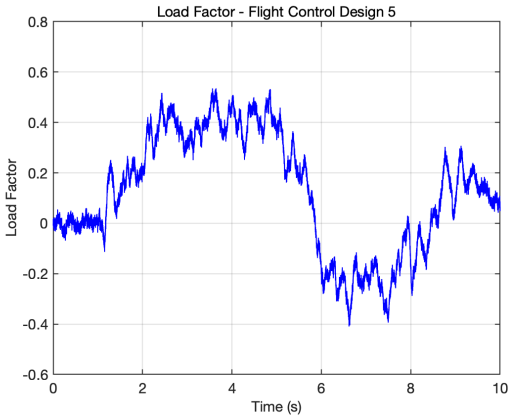

(d) Load Factor - Flight Control Design 5

Figure 20. Load Factor Comparison

6. *Flight Control Design 6: Flight Path Angle - Acceleration Suppression - Gust Load Alleviation Control with No Gust Estimation*

The effect of gust estimation is examined next. Gust disturbance estimation adds another layer of complexity in the flight control design. Robustness and stability are required for gust estimation. The stability of the gust estimation can be established as shown previously. In all the flight control simulations above, gust estimation is implemented with $\Gamma_r = 10I$, $\Gamma_e = 10I$, $\sigma_r = 0.1$, $\sigma_e = 0$, $\mu_r = 1$, and $\mu_e = 0$. To examine the effect of gust estimation, it is turned off in flight control design 6. Figure 21(a) shows the angle of attack which substantially increases over those with the other flight control designs. Concomitantly, the fuselage vertical accelerations also significantly increase to a similar level as that with flight control design 2 as shown in Fig. 22(a), thereby nullifying the benefit of the acceleration suppression control. The effects of gust estimation on the modal response and wing tip vertical accelerations are minimal as seen in Figs. 21(a) and 22(b). The reason for this becomes apparent in Figs. 23(a) and 23(b). The two fuselage accelerometers can provide a full-rank estimation of the gust disturbance in the angle of attack and pitch rate dynamics. Figure 23(a) shows the gust estimate for the angle of attack dynamics. The estimation is not by any means accurate. Yet, the effect on the flight control design is seen to be very beneficial. On the other hand, using the only two wing tip accelerometers, the gust estimation is not a full-rank estimation. That is, there are as many accelerometers as there are the number of modes to be estimated in a full-rank estimation. Therefore, the estimation is in a least-squares sense using a pseudo-inverse. As a result, the gust estimation for the flexible wing structural dynamics is rather ineffective. This is seen in 23(b). Thus, the beneficial effect of the gust estimation is derived mostly from reducing the effect of the gust contribution in the rigid-body flight dynamics.

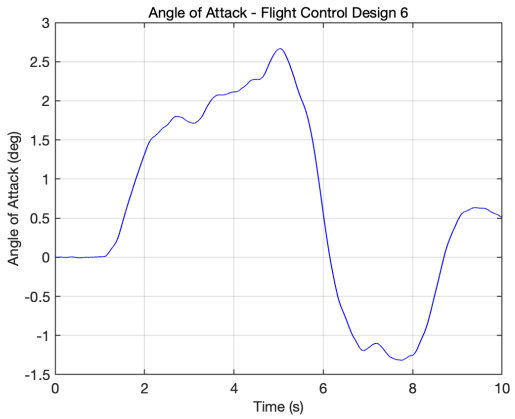

(a) Angle of Attack

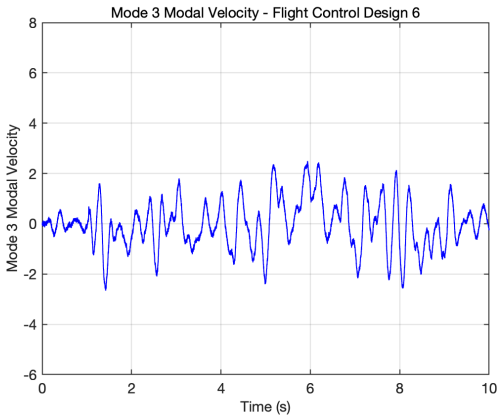

(b) Mode 1 Modal Velocity

Figure 21. Angle of Attack and Modal Velocity - Flight Control Design 6

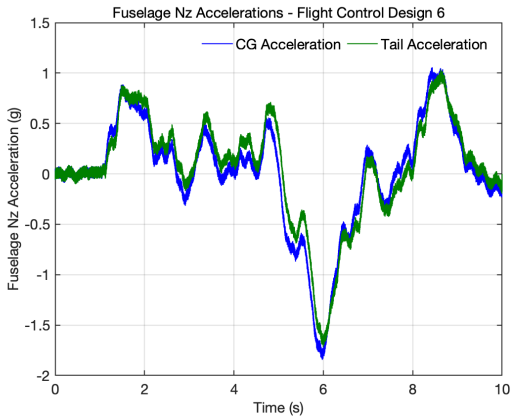

(a) Aircraft Fuselage Vertical Accelerations

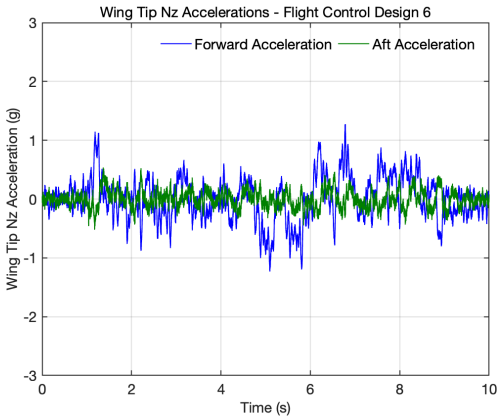

(b) Wing Tip Vertical Accelerations

Figure 22. Aircraft Fuselage and Wing Tip Vertical Accelerations - Flight Control Design 6

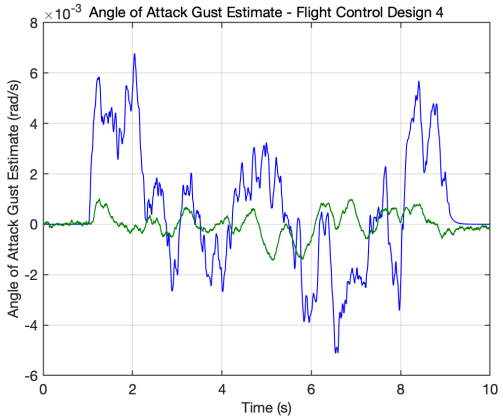

(a) Gust Estimate for Angle of Attack Dynamics

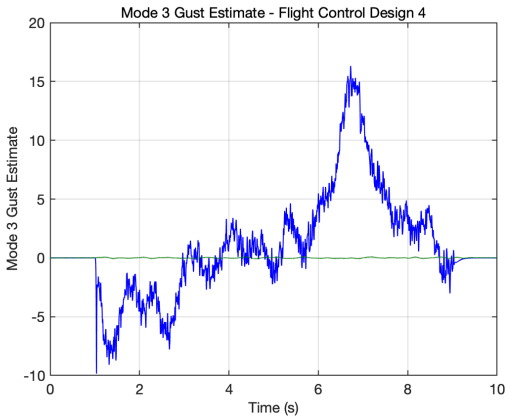

(b) Gust Estimate for Mode 3 Dynamics

Figure 23. Gust Estimates for Angle of Attack and Mode 3 Dynamics - Flight Control Design 4

C. Ride Quality Assessments

In the study by Leatherwood, Dempsey, and Clevenson,[1] the authors propose a ride discomfort metric for random vibration

$$DISC = \begin{cases} a + bX_{rms} & X_{rms} \geq X^*_{rms} \\ cX_{rms} & X_{rms} < X^*_{rms} \end{cases} \tag{57}$$

where $X^*_{rms} = 0.02g_{rms}$, and the coefficients a, b, and c are listed Table 3 of this study in three groups corresponding to three frequency bandwidths of @ Hz, 5 Hz, and 10 Hz.

The discomfort metric which is a function of the cabin acceleration frequencies and RMS levels provides a convenient means for conducting ride quality assessments of the flight control designs above. Thus, the two fuselage accelerations at the aircraft CG and the tail will be used in this study. Table 3(a) of the referenced study[1] shows the values of the coefficients a, b, and c at various center frequencies up to 13 Hz and frequency bandwidths up to 10 Hz for the vertical acceleration. The maximum frequency for the 13 Hz center frequency and 10 Hz frequency bandwidth is 18 Hz which is below the frequency of 19.47 Hz of mode 10 in the aircraft model (see Table 2). Therefore, the aircraft model provides a sufficient frequency bandwidth for ride quality assessments.

The fuselage accelerations for the six flight control designs are transformed into the frequency domain via a fast Fourier transform (FFT). Figures 24(a) and 24(b) show the spectra of the fuselage CG and fuselage tail vertical accelerations. The largest frequency responses for both the fuselage CG and fuselage tail occur at 0.3 Hz which corresponds to the frequency of the short-period mode. At a glance, flight control design 5 has larger peaks than the other flight control designs. Flight control design 2 also shows the largest peak at 2.1 Hz. Flight control design 3 has lower peaks than the other flight control designs.

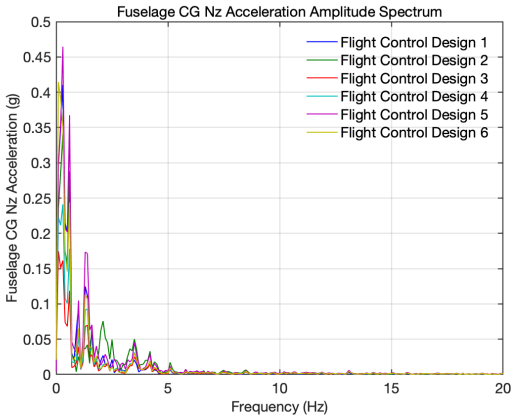

(a) Fuselage CG Vertical Acceleration Spectrum

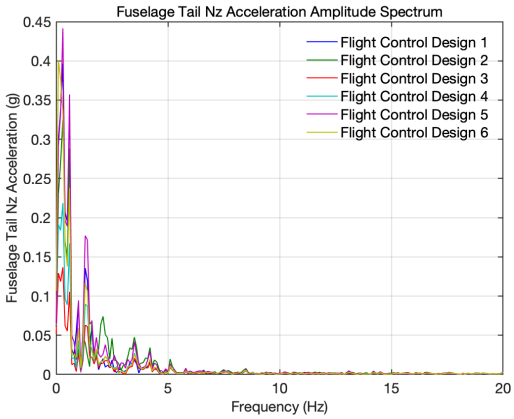

(b) Fuselage Tail Vertical Acceleration Spectrum

Figure 24. Fuselage Vertical Acceleration Spectra

The discomfort metrics are evaluated at the fuselage CG and fuselage tail for the three frequency bandwidths. The maximum discomfort metrics at a given frequency are then computed by taking the maximum of the discomfort metrics for the three frequency bandwidths. Figures 25(a)-25(d) are for plots of the discomfort metrics at the fuselage CG. Figures 26(a)-26(d) are the plots of the discomfort metrics at the fuselage tail. Figures 25 and 26 look very similar. This suggests that the ride qualities at the fuselage CG and fuselage tail are nominally the same. The different frequency bandwidths give rise to different discomfort metrics, but the trends look similar and clearly show that flight control design 2 provides the worst ride quality. Flight control design 5 also performs poorly in terms of ride quality. Flight control design 3 provides the best ride quality. This flight control design has the acceleration suppression control which clearly provides the ride quality improvement over the other flight control designs.

The referenced study also suggests a within-axis discomfort index by taking the square root of the sum of the squares of the maximum discomfort metrics at the individual frequencies. This is a cumulative discomfort metric within a single axis over the frequency range of interest and is given by

$$DISC_{vert} = \sqrt{\sum_{i}^{N} DISC_i} \tag{58}$$

where N is the number of frequencies.

Figures 27(a) and 27(b) show the cumulative discomfort metrics at the fuselage CG and fuselage tail for the six flight control designs. This figure clearly shows that both flight control designs 2 and 5 have the worst ride qualities. The best ride quality is provided by flight control design 3 and the next best ride quality is provided by flight control design 4. Flight control design 2 is the conventional single-objective flight path angle control with only the elevator as the control surface. Flight control design 5 is a three-objective flight path angle - acceleration suppression - gust load alleviation control and is the same as flight control design 4, except that it has a 10 times more gust load alleviation weighting. Thus, this suggests the some amount of gust load alleviation is necessary for ride quality, but too much of it could cause an unintended effect. The results also show that the acceleration suppression control is essential in providing good ride quality. This is not a surprising conclusion since the discomfort metrics are a function of the accelerations and frequencies.

It should be noted that ride quality depends on other factors beside just the acceleration levels. Transmissibility of aircraft seats and the vibration of interior structures as a result of load transmissions into the cabin are other factors contributing to ride quality. This study does not account for those effects and the conclusion is relative to the present flight control study.

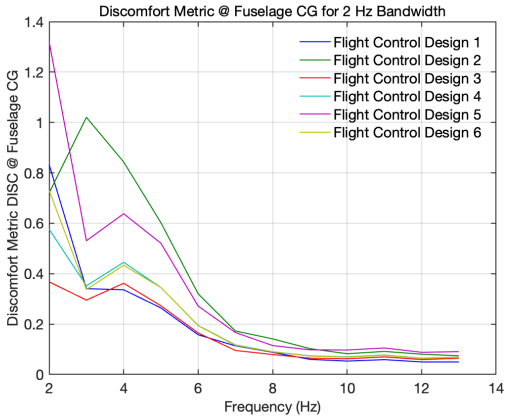

(a) Discomfort Metrics @ Fuselage CG for 2 Hz Bandwidth

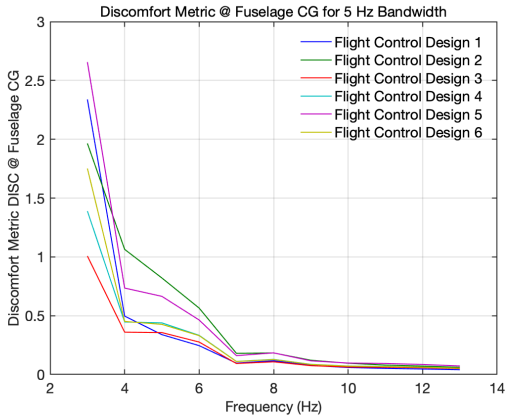

(b) Discomfort Metrics @ Fuselage CG for 5 Hz Bandwidth

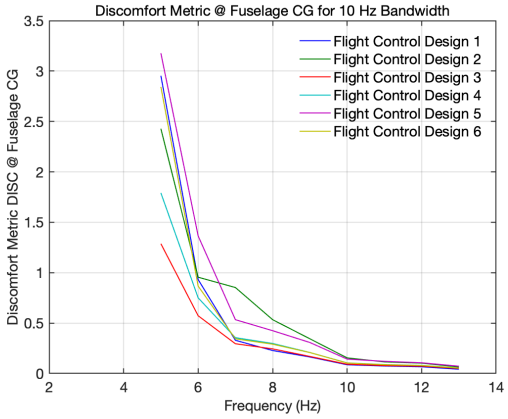

(c) Discomfort Metrics @ Fuselage CG for 10 Hz Bandwidth

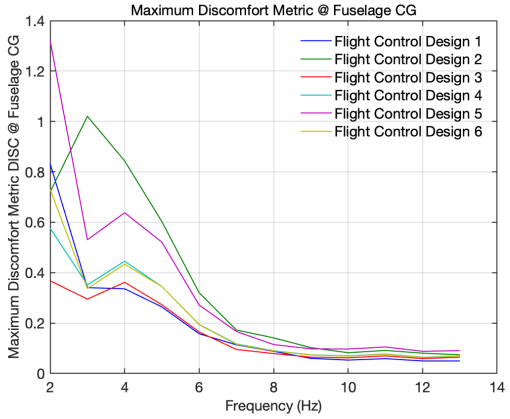

(d) Maximum Discomfort Metrics @ Fuselage CG

Figure 25. Discomfort Metrics @ Fuselage CG

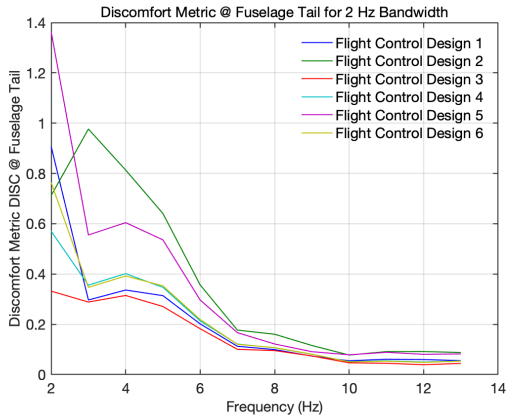

(a) Discomfort Metrics @ Fuselage Tail for 2 Hz Bandwidth

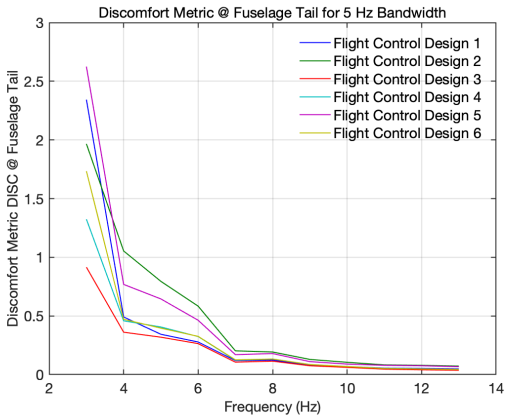

(b) Discomfort Metrics @ Fuselage Tail for 5 Hz Bandwidth

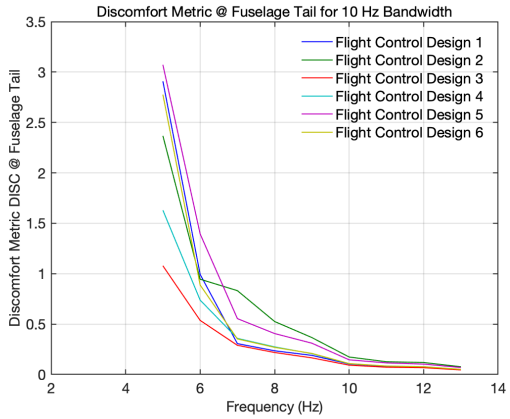

(c) Discomfort Metrics @ Fuselage Tail for 10 Hz Bandwidth

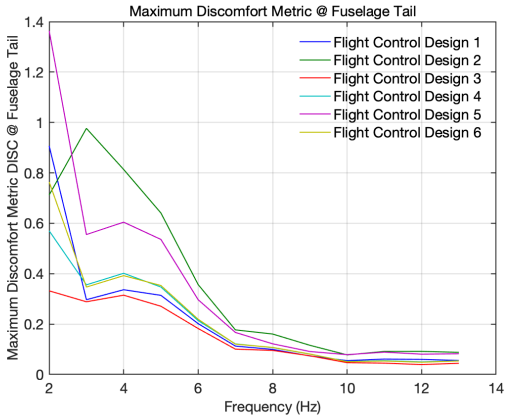

(d) Maximum Discomfort Metrics @ Fuselage Tail

Figure 26. Discomfort Metrics @ Fuselage Tail

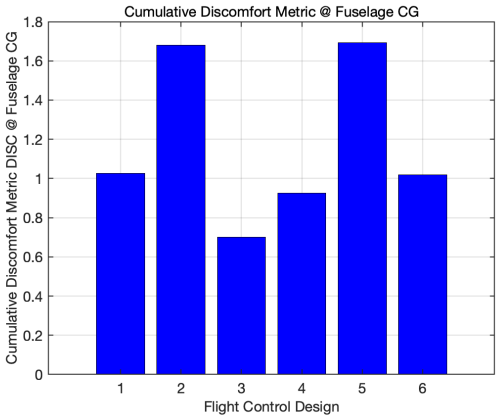

(a) Cumulative Discomfort Metrics @ Fuselage CG

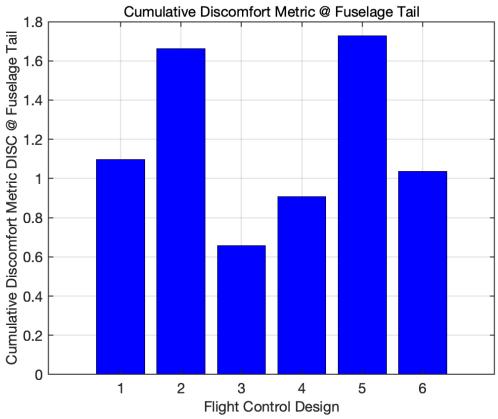

(b) Cumulative Discomfort Metric @ Fuselage Tail

Figure 27. Cumulative Discomfort Metrics for Vertical Motion

V. Conclusion

This paper presents a multi-objective flight control design for improved ride quality of flexible transport aircraft. A multi-objective flight control design is proposed to include an acceleration suppression control along with a gust load

alleviation control in a flight control system design to help improve ride quality of flexible aircraft. A gust estimation approach is developed. Six different flight control designs are simulated for a flexible wing generic transport model. Ride quality assessments are conducted by evaluating discomfort metrics developed by earlier researchers. The study shows that the acceleration suppression control provides the most improved ride quality among the flight control designs. The study also shows that some amount of gust load alleviation is necessary to reduce load transmissions to improve ride quality, but when it outweighs the acceleration suppression in a multi-objective flight control setting, an opposite effect is a result. The study also suggests that for flexible aircraft the conventional single-axis flight control design using only the elevator in the pitch axis may not provide good ride quality during a severe turbulence or gust encounter. Flight control surfaces on the wing are necessary to provide more control authority to suppress the aircraft vertical acceleration than the conventional flight control surfaces.

Acknowledgment

The authors would like to thank the Advanced Air Transport Technology Project under the Advanced Air Vehicles Program of NASA Aeronautics Research Mission Directorate (ARMD) for funding support of this work.

References

[1]Leatherwood, J. D., Dempsey, T. K., and Clevenson, S. A., "A Design Tool for Estimating Passenger Ride Discomfort Within Complex Ride Environments," Human Factor, Vol. 22, No. 3, pp. 291-312, June 1980.

[2]Nguyen, N., Ting, E., and Chaparro, D., "Development of an Integrated Nonlinear Aeroservoelastic Flight Dynamic Model of the NASA Generic Transport Model," AIAA/ASCE/AHS/ASC Structures, Structural Dynamics, and Materials Conference, AIAA-2018-2210, January 2018.

[3]Nguyen, N. and Tal, E., "A Multi-Objective Flight Control Approach for Performance Adaptive Aeroelastic Wing," 56th AIAA/ASME/ASCE/AHS/SC Structures, Structural Dynamics, and Materials Conference, AIAA-2015-1843, January 2015.

[4]Nguyen, N., Ting, E., Chaparro, D., Drew, M., and Swei, S., "Multi-Objective Flight Control for Drag Minimization and Load Alleviation of High-Aspect Ratio Flexible Wing Aircraft," 58th AIAA/ASME/ASCE/AHS/SC Structures, Structural Dynamics, and Materials Conference, AIAA-2017-1589, January 2017.

[5]Hashemi, K., Nguyen, N., Drew, M., Ting, E., and Chaparro, D., "Performance Optimizing Gust Load Alleviation Control of Flexible Wing Aircraft," AIAA Guidance, Navigation, and Control Conference, AIAA-2018-0623, January 2017.

[6]Ferrier, Y., Nguyen, N., Ting, E., Chaparro, D., Wang, X., de Visser, C., and Chu, Q., "Active Gust Load Alleviation of High-Aspect Ratio Flexible Wing Aircraft," AIAA Guidance, Navigation, and Control Conference, AIAA-2018-0620, January 2017.

[7]Nguyen, N., Hashemi, K., and Drew, M., "Multi-Objective Adaptive Control for Load Alleviation and Drag Minimization of Flexible Aircraft," AIAA Guidance, Navigation, and Control Conference, AIAA-2018-0622, January 2018.

[8]Drew, M., Hashemi, K., Cramer, N., and Nguyen, N., "Multi-Objective Optimal Control of the 6-DoF Aeroservoelastic Common Research Model with Aspect Ratio 13.5 Wing," AIAA Structural Dynamics Conference, AIAA-2019-0220, January 2019.

[9]Nguyen, N., "Elastically Shaped Future Air Vehicle Concept," NASA Innovation Fund Award 2010 Report, October 2010, Submitted to NASA Innovative Partnerships Program, http://ntrs.nasa.gov/archive/nasa/casi.ntrs.nasa.gov/20110023698.pdf

[10]Nguyen, N. and Urnes, J., "Aeroelastic Modeling of Elastically Shaped Aircraft Concept via Wing Shaping Control for Drag Reduction," AIAA Atmospheric Flight Mechanics Conference, AIAA-2012-4642, August 2012.

[11]Nguyen, N., Trinh, K., Reynolds, K., Kless, J., Aftosmis, M., Urnes, J., and Ippolito, C., "Elastically Shaped Wing Optimization and Aircraft Concept for Improved Cruise Efficiency," AIAA Aerospace Sciences Meeting, AIAA-2013-0141, January 2013.

[12]Urnes, J., Nguyen, N., Ippolito, C., Totah, J., Trinh, K., and Ting, E., "A Mission Adaptive Variable Camber Flap Control System to Optimize High Lift and Cruise Lift to Drag Ratios of Future N+3 Transport Aircraft," AIAA Aerospace Sciences Meeting, AIAA-2013-0214, January 2013.

[13]Nguyen, N., Lebofsky, S., Ting, E., Kaul, U., Chaparro, D., and Urnes, J., "Development of Variable Camber Continuous Trailing Edge Flap for Performance Adaptive Aeroelastic Wing," SAE AeroTech Congress & Exhibition, 15ATC-0250 / 2015-01-2565, September 2015.

[14]Ferrier, Y., Nguyen, N., and Ting, E., "Real-Time Adaptive Least-Squares Drag Minimization for Performance Adaptive Aeroelastic Wing," 34th AIAA Applied Aerodynamics Conference, AIAA-2016-3159, June 2016.

[15]Nguyen, N., Cramer, N., Hashemi, K., Drew, M., Wise, R., Boskovic, J., Mundt, T., Precup, N., and Livne, E., "Real-Time Adaptive Drag Minimization Wind Tunnel Investigation of a Flexible Wing with Variable Camber Continuous Trailing Edge Flap System," AIAA Applied Aerodynamic Conference, AIAA-2019-3156, June 2019.

[16]Jordan, T. L., Langford, W. M., Belcastro, C. M., Foster, J. M., Shah, G. H., Howland, G., and Kidd, R., "Development of a Dynamically Scaled Generic Transport Model Testbed for Flight Research Experiments," AUVSI Unmanned Unlimited, Arlington, VA, 2004.

[17]Nguyen, N., Krishnakumar, K., Kaneshige, J., and Nespeca, P., "Flight Dynamics Modeling and Hybrid Adaptive Control of Damaged Asymmetric Aircraft," AIAA Journal of Guidance, Control, and Dynamics, Vol. 31, No. 3, pp. 751-764, March 2008.

[18]Nguyen, N., Krishnakumar, K., Kaneshige, J., and Nespeca, P., "Dynamics and Adaptive Control for Stability Recovery of Damaged Asymmetric Aircraft," AIAA Guidance, Navigation, and Control Conference, AIAA-2006-6049, August 2006.

[19]Nguyen, N., Ting, E., Nguyen, D., and Trinh, K., "Flutter Analysis of Mission-Adaptive Wing with Variable Camber Continuous Trailing Edge Flap," 55th AIAA/ASME/ASCE/AHS/ASC Structures, Structural Dynamics, and Materials Conference, AIAA-2014-0839, January 2014.